

TinyDef-DETR: A Transformer-Based Framework for Defect Detection in Transmission Lines from UAV Imagery

Feng Shen ¹, Jiaming Cui ¹, Wenqiang Li ¹, and Shuai Zhou ^{1,2*}

¹ Harbin Institute of Technology, Harbin 150001, China;

fshen@hit.edu.cn(F.S.); hitcjm@stu.hit.edu.cn(J.C.); wenqli@stu.hit.edu.cn(W.L.); 22B901046@stu.hit.edu.cn(S.Z.)

² Electric Power Research Institute, Yunnan Power Grid Co., Ltd., Kunming 650217, China; 22B901046@stu.hit.edu.cn(S.Z.)

* Correspondence: 22B901046@stu.hit.edu.cn (S.Z.)

Highlights

What are the main findings?

- We propose **TinyDef-DETR**, a transformer-based detection framework specifically designed for UAV imagery in transmission line defect detection, integrating edge-enhanced feature extraction, stride-free space-to-depth downsampling, dual-domain multi-scale attention, and a Focaler-Wise-SIoU loss function.

What is the implication of the main finding?

- The proposed framework enhances the reliability and scalability of UAV-based transmission line defect detection, enabling efficient defect analysis with low computational requirements and reducing missed detections in field deployments.
- The design principles of TinyDef-DETR demonstrate a certain level of generalizability in improving small-object detection performance, particularly in remote sensing and aerial vision applications.

Abstract

Automated defect detection from UAV imagery of transmission lines is a challenging task due to the small size, ambiguity, and complex backgrounds of defects. This paper proposes TinyDef-DETR, a DETR-based framework designed to achieve accurate and efficient detection of transmission line defects from UAV-acquired images. The model integrates four major components: an edge-enhanced ResNet backbone to strengthen boundary-sensitive representations, a stride-free space-to-depth module to enable detail-preserving downsampling, a cross-stage dual-domain multi-scale attention mechanism to jointly model global context and local cues, and a Focaler-Wise-SIoU regression loss to improve the localization of small and difficult objects. Together, these designs effectively mitigate the limitations of conventional detectors. Extensive experiments on both public and real-world datasets demonstrate that TinyDef-DETR achieves superior detection performance and strong generalization capability, while maintaining modest computational overhead. The accuracy and efficiency of TinyDef-DETR make it a suitable method for UAV-based transmission line defect detection, particularly in scenarios involving small and ambiguous objects.

Keywords: Transmission lines; Defect detection; UAV imagery; Small Object Detection;

arXiv:2509.06035v8 [cs.CV] 3 Nov 2025

Received:

Revised:

Accepted:

Published:

Citation: Shen, F.; Cui, J.; Li, W.; Zhou, S. TinyDef-DETR: UAV-Based Transmission Lines Defect Detection. *Remote Sens.* **2025**, *1*, 0. <https://doi.org/>

Copyright: © 2025 by the authors. Submitted to *Remote Sens.* for possible open access publication under the terms and conditions of the Creative Commons Attribution (CC BY) license (<https://creativecommons.org/licenses/by/4.0/>).

1. INTRODUCTION

Along with the sustained development of the Chinese economy, the mileage of transmission lines has increased rapidly[1]. As the core infrastructure for long-distance energy transmission, their reliable operation is essential for meeting the growing demand for electricity[2]. However, transmission lines are exposed to harsh outdoor environments[3], where prolonged exposure significantly raises the risk of diverse faults—ranging from component damage to foreign object intrusions—collectively referred to as transmission line defects[4].

Unmanned aerial vehicles (UAVs) are increasingly employed to capture imagery of transmission lines for post-flight visual inspection and defect detection[5]. In such UAV-acquired imagery, defects often appear as small objects due to long shooting distances and the inherent resolution limitations of aerial imaging systems[6]. These small objects typically occupy regions smaller than 32×32 pixels, lacking clear contours and distinct textures, which severely hampers reliable recognition[7]. The challenge is further exacerbated by complex backgrounds such as vegetation, towers, and shadows, where small defects are frequently obscured or confused with surrounding structures[8].

With the rapid advancement of smart grid development, transmission line defect detection has increasingly adopted deep learning-based object detection methods[9]. Alongside this progress, numerous general-purpose detectors—such as YOLO[10], DINO[11], and RT-DETR[12]—have been developed. While these models achieve remarkable success in generic scenarios, most of them on the COCO dataset[13], they face notable limitations in transmission line defect detection under complex conditions involving occlusion, background clutter, and variable lighting[14]. Common issues include missed detections, false positives, and false negatives, which substantially undermine the practical utility of UAV-acquired imagery in real-world transmission line maintenance[15]. These shortcomings are consistently reported in previous studies and further confirmed by our preliminary experiments, highlighting the critical need for specialized detection frameworks capable of accurately identifying small-scale defects in UAV operational scenarios.

In this article, we propose TinyDef-DETR, a novel transmission line defect detection network built upon the Transformer[16] architecture, which aims to enhance detection accuracy, recall, and robustness for UAV-acquired imagery under complex inspection scenarios. The main contributions of this work are summarized as follows:

1. We construct an Edge Enhanced ResNet (EE-ResNet) by embedding an Edge-Enhanced Convolution (EEConv) module into the residual backbone. The EEConv integrates central, horizontal, and vertical difference convolutions to encode gradient priors, thereby improving sensitivity to fine-grained details and object boundaries. Through a re-parameterization strategy, the multi-branch structure of EEConv is fused into a single 3×3 kernel at inference, incurring no additional computational overhead. By augmenting the ResNet backbone with such edge-aware feature extraction, EE-ResNet substantially strengthens the representation capability for small-scale defects in UAV inspection imagery.
2. We introduce a stride-free downsampling module based on space-to-depth transformation, which reorganizes spatial information into the channel dimension using a fixed 2×2 partition without stride convolution. This design preserves pixel-level details while reducing spatial resolution, thereby improving recall for extremely small defects that are often missed by conventional strided convolution architectures.
3. We propose a lightweight attention block with a dual-domain FSCA (Frequency-Spatial-Channel Attention) mechanism, integrated in a cross-stage partial manner. This design jointly enhances global semantic reasoning and local detail preservation,

enabling the network to better capture anisotropic defect patterns such as missing bolts, loose clamps, and sagging wires.

4. We develop a novel Focaler-Wise-SIoU loss that combines normalized IoU scaling, Scylla-IoU geometric penalties, and non-monotonic focal modulation. This adaptively emphasizes moderately difficult samples while suppressing trivial or noisy ones, thereby stabilizing training and improving localization accuracy for small-scale defect regions.

2. Related Works

2.1. Applications of Transformer-Based Model in Power Line Defect Detection

Tian et al.[17] addressed the challenge of insulator defect detection in low-quality UAV imagery by introducing a patch-based diffusion model for image restoration and an optimized DETR with Spatial Information Interaction and Feature Convergence Modules, achieving superior detection accuracy of 95.8% particularly for small defects, while the limitations lie in incomplete coverage of defect types, restricted generalization across diverse grid structures, and computational inefficiency in real-time applications, primarily due to dataset constraints and model complexity. Cheng and Liu successively advanced Transformer-based approaches for insulator defect detection by first enhancing DETR[18] with refined attention and feature optimization to improve localization accuracy over the baseline, and later proposing AdIn-DETR[3] with lightweight feature fusion and task-specific adaptation for real-time end-to-end detection, achieving superior precision–efficiency trade-offs, though both methods remain limited by reduced robustness under complex backgrounds and unseen categories, largely due to dataset insufficiency and the inherent constraints of Transformer complexity and speed. Wang et al.[19] developed a Transformer-based detection framework for advanced insulator defect identification, integrating multi-scale feature enhancement and context-aware attention to improve recognition accuracy and robustness, achieving state-of-the-art reliability in complex grid environments, while the model still suffers from efficiency limitations and reduced adaptability to rare defect patterns, mainly due to computational overhead and the scarcity of diverse annotated datasets. Xie et al.[20] proposed Power-DETR, a Transformer-based end-to-end detection framework for power line defect components, in which contrastive denoising learning and a hybrid query selection strategy were introduced to enhance small-object recognition and detection robustness, achieving superior accuracy over baseline DETR, yet the method still faces challenges in computational efficiency and generalization to highly variable field conditions, mainly due to increased model complexity and limited dataset diversity. Yang and Wang [4] proposed a hybrid detection framework combining YOLOv5 with Transformer-based DETR to recognize bird nests on transmission lines from small-sample datasets, introducing transfer learning and data augmentation to mitigate limited training data, which achieved reliable detection performance under constrained scenarios, while its limitation lies in reduced scalability and robustness for large-scale deployments, mainly due to dataset scarcity and the trade-off between lightweight training and generalization capacity.

2.2. Joint Frequency–Spatial Representations for Small Object Detection

A growing body of work argues that purely spatial attention is insufficient for detecting small, weak, and cluttered targets, and instead advocates *joint frequency–spatial* representations that explicitly preserve high-frequency cues while suppressing background aliasing and downsampling loss. Representative approaches inject wavelet- or spectrum-domain operators into DETR/YOLO backbones: for instance, replacing standard operators with wavelet-domain anti-aliasing and convolution improves fine-structure perception and

multi-scale representation under real-time constraints [21]. In infrared small-target detection, Haar wavelet decompositions have been used to derive high-/low-frequency masks that selectively retain fine details and mitigate over-smoothing, achieving state-of-the-art performance and illustrating an “frequency-guides-spatial” paradigm [22]; subsequent designs integrate frequency–spatial convolutions and cross-domain attention to highlight local high-frequency details while using low frequencies to complete global structure, yielding consistent gains with lightweight models [23]. From the feature fusion perspective, frequency-gated attention strengthens high-frequency details that are easily drowned out by deep downsampling, and combining it with grouped spatial–channel transformers produces robust small-target descriptors [24]; similarly, explicitly separating and re-fusing spatial and frequency channels in hierarchical transformers alleviates the loss of detail caused by aggressive subsampling and semantics-dominant deep layers [25]. Importantly, these studies also caution that frequency interaction is not “the more the better”: without proper masking or dynamics modeling, it may amplify boundary noise; coupling frequency-interaction attention with stabilizing mechanisms has been shown to suppress irrelevant high-frequency artifacts and emphasize targets nearly indistinguishable from background [26]. Beyond wavelets, discrete cosine transform (DCT) features, aligned and fused with spatial cues, have improved AP for small objects in remote sensing, indicating that cosine-spectrum bases offer complementary discriminative power for tiny structures [27]. Earlier frequency/multi-resolution methods (e.g., NSCT/Contourlet families) have also informed background estimation and low-frequency isolation: isolating low-frequency components reduces sensor and clutter noise while high-frequency components recover target details, providing a principled route to boost the small-target signal-to-noise ratio [28,29]. In UAV scenarios emphasizing on-board efficiency, integrating wavelet convolutions and lightweight attention into real-time DETR variants demonstrates stable gains on diminutive, high-altitude objects and underscores the efficacy of “frequency-aware convolutions + transformers” under embedded constraints [30].

In summary, the literature converges on three lessons. First, frequency decomposition should be paired with spatial alignment or masking to suppress noisy high-frequency components [22,26]. Second, coupling with multi-scale or large-receptive-field modules is crucial to balance local details and global context [21,23]. Finally, the practical impact depends on lightweight implementations suitable for UAV platforms[30].

3. Methods

3.1. Overview

In this study, we employ RT-DETR-r18[12] as the baseline detection framework owing to its superior accuracy and robustness in complex scenarios. Compared with traditional DETR models, RT-DETR exhibits significantly faster training convergence and improved deployment efficiency, making it more suitable for real-time and resource-constrained applications such as UAV-based inspection tasks [31].

RT-DETR incorporates an enhanced encoder–decoder architecture together with refined query interaction mechanisms, while for the backbone network, RT-DETR-r18 adopts a CNN-based design, namely the popular ResNet-18[32]. From the perspective of real-time performance, employing a CNN architecture for feature extraction further enhances the real-time capability of DETR-like models, thereby improving their practical applicability. As a result, RT-DETR not only accelerates convergence and improves detection precision, but also preserves the global context modeling capability of Transformer-based frameworks[16]. In addition, its lightweight optimization strategies—specifically, the design choice to apply the encoder only to high-level semantic features (S5) with relatively small spatial dimensions—effectively reduce resource consumption. This balances performance

and speed by significantly decreasing computational overhead and accelerating inference without compromising accuracy, thereby making RT-DETR particularly suitable for post-flight UAV imagery analysis, where large volumes of data must be processed efficiently under computational and energy constraints[17].

By contrast, YOLO-based detectors, though widely favored for their real-time efficiency and ease of deployment[33], tend to degrade in performance when handling small, occluded, or densely distributed objects, owing to their anchor-dependent design and limited global receptive field. This aligns with the findings of Ismail et al.[34], who reported that while YOLO excels in real-time scenarios, it struggles with small-object detection and occlusion, whereas DETR achieves higher accuracy in complex environments at the cost of greater computational demand. Our preliminary experiments further compared RT-DETR with representative YOLO series models, including YOLOv3[35], YOLOv7[36], and YOLO 11[37], and showed that RT-DETR consistently outperformed most of them in overall performance. In cases where certain YOLO variants (e.g., YOLO 11m) surpassed RT-DETR, their gains were typically accompanied by substantially larger parameter sizes, thereby underscoring RT-DETR's advantageous balance between model complexity and detection accuracy.

Taken together, the consistent advantages of RT-DETR over both traditional DETR models and representative YOLO series substantiate its adoption as the baseline framework in this study.

Building upon this strong foundation, we propose TinyDef-DETR as a dedicated solution for small object defect detection in UAV-based transmission line inspection. The overall architecture is illustrated in Fig.1.

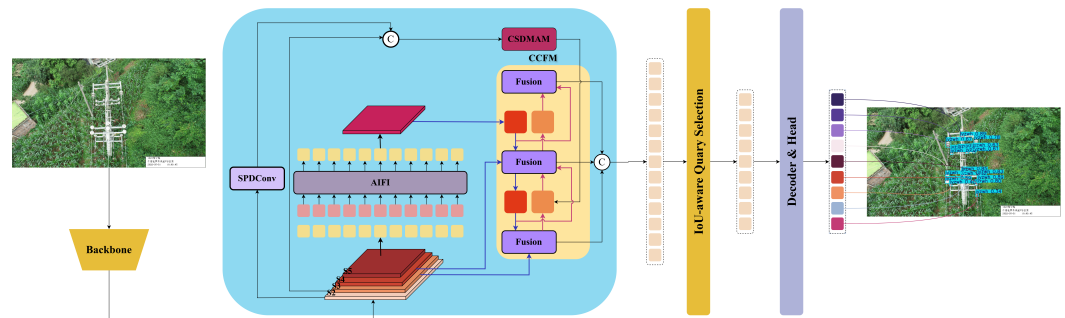


Figure 1. Overall framework of TinyDef-DETR

First, the backbone adopts the Edge-Enhanced ResNet (EE-ResNet) structure to strengthen low-level detail preservation. Second, a compact Space-to-Depth Convolution (SPD) module is inserted before each downsampling layer to reorganize spatial features in a manner that preserves critical spatial information while reducing resolution, thereby improving the recall rate of extremely small objects. Third, a lightweight Cross-Stage Dual-Domain Multi-Scale Attention Module (CSDMAM) is embedded into the backbone network to enhance directional sensitivity and fine-grained structural modeling, effectively capturing anisotropic features of typical defects such as missing bolts, loose clamps, or sagging wires. Finally, a Focaler-Wise-SIoU loss function is employed to jointly optimize classification and localization. This loss function adaptively balances easy and hard samples while providing more accurate bounding box regression through shape-aware optimization, which further improves detection robustness for small and ambiguous objects. Detailed descriptions of the proposed modules can be found in Sections 3.2 to 3.5.

3.2. Edge Enhanced ResNet

ResNet[32] represents a milestone in deep learning for computer vision, introducing residual learning that enables the effective training of very deep networks. Owing to

its simple yet modular design, it has become a widely adopted backbone across a broad spectrum of vision tasks. Nevertheless, when applied to UAV-based visual inspection for transmission line defect detection, native ResNet architectures, as verified in preliminary experiments, exhibit limited capability in capturing sufficiently fine-grained features, thereby constraining their effectiveness in identifying small and subtle defect objects, particularly in challenging transmission line inspection environments with interference from vegetation, man-made structures, and adjacent electrical installations.

Inspection of the heatmaps exported from ResNet further reveals that they lack clear edges and fine contours, which exacerbates the difficulty of accurately localizing subtle defects. Unlike conventional convolution, where the high performance of CNN-based edge feature extraction typically relies on large pretrained backbones—resulting in high memory consumption and energy cost, which contradicts the real-time requirements of UAV-based transmission line defect detection tasks—difference convolution introduces differential operations to enhance sensitivity to gradient variations and fine-grained structural details, thereby improving the extraction of local details and object boundaries[38].

To address the aforementioned problem, we propose an EEConv (edge enhancement convolution). Building on this idea, EEConv explicitly incorporates three difference convolution operators—central difference convolution (CDC), horizontal difference convolution (HDC), and vertical difference convolution (VDC)—to embed gradient priors into the feature extraction process. The overall structure of EEConv is illustrated in Fig. 2(a). To ensure deployment efficiency, EEConv adopts a re-parameterization strategy that fuses its multi-branch convolutions into a single equivalent 3×3 kernel during inference. Once fused, the auxiliary branches are discarded, leaving only a lightweight standard convolution. This allows the module to preserve the expressive power gained from multi-branch training while maintaining the same computational cost as a vanilla convolution. During deployment, the structure of EEConv becomes as shown in Fig. 2(b).

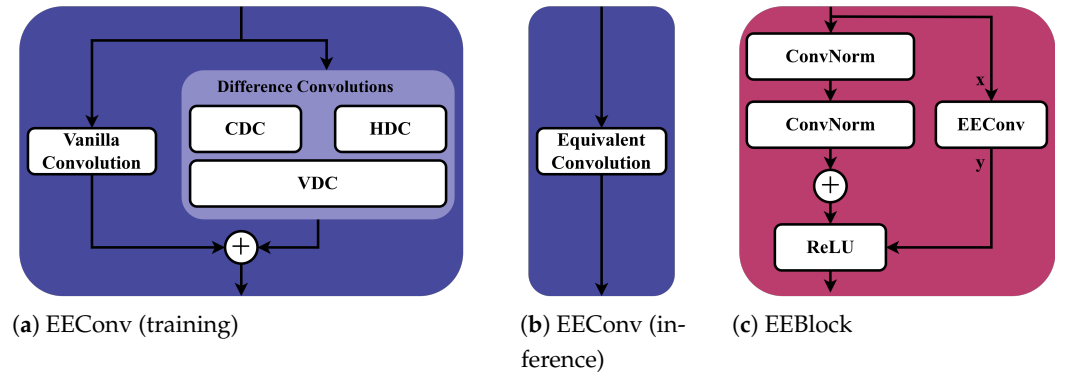


Figure 2. The architecture of EEBlock (Edge Enhanced Block)

Formally, let the four convolutional branches be denoted as (W_k, b_k) , $k = 1, 2, 3, 4$, corresponding to CDC, HDC, VDC, and the Vanilla convolution, respectively. During training, their weights and biases are linearly aggregated to obtain an equivalent 3×3 kernel and bias:

$$W_{\Sigma} = \sum_{k=1}^4 W_k,$$

$$b_{\Sigma} = \sum_{k=1}^4 b_k.$$

The intermediate feature map is then obtained as

$$z = \text{Conv}_{3 \times 3}(x; W_{\Sigma}, b_{\Sigma}),$$

followed by batch normalization and a non-linear activation $\phi(\cdot)$:

$$y = \phi\left(\gamma \cdot \frac{z - \mu}{\sqrt{\sigma^2 + \epsilon}} + \beta\right).$$

For inference, the BN parameters are absorbed into the convolution kernel, yielding per-channel scaling:

$$\alpha_c = \frac{\gamma_c}{\sqrt{\sigma_c^2 + \epsilon}},$$

and the final equivalent kernel and bias are computed as

$$\begin{aligned} W_c^{(\text{final})} &= \alpha_c \cdot W_{\Sigma, c}, \\ b_c^{(\text{final})} &= \alpha_c \cdot (b_{\Sigma, c} - \mu_c) + \beta_c. \end{aligned}$$

Thus, during deployment, EEConv degenerates into a single 3×3 convolution followed by activation:

$$y = \phi\left(\text{Conv}_{3 \times 3}(x; W^{(\text{final})}, b^{(\text{final})})\right),$$

which guarantees equivalence with the training-time formulation while ensuring zero additional inference overhead.

To integrate this into our framework, we replace the second 3×3 convolution in the residual branch of standard ResNet basic blocks with EEConv, thereby preserving the backbone's modular design while substantially improving sensitivity to fine-grained structures. This design choice is motivated by the observation that the second 3×3 convolution in each residual block primarily functions as a feature refiner, responsible for aggregating local structural details after the first convolution has extracted preliminary features. In this way, we obtain the Edge-Enhanced Block (EEBlock), whose structure is illustrated in Fig. 2(c).

By substituting the refining convolution with EEConv, we embed directional gradient priors precisely at the stage where fine-grained information is consolidated, thus maximizing the impact of EEConv on enhancing edge and detail representation. Meanwhile, the first 3×3 convolution and the shortcut connection remain unchanged, ensuring full compatibility with the original ResNet architecture and preserving its residual learning mechanism.

Integrating EEBlocks throughout the backbone yields the Edge-Enhanced ResNet (EE-ResNet), which significantly improves sensitivity to subtle structural details while maintaining computational efficiency. EE-ResNet provides a robust feature extraction foundation, offering stronger boundary-aware representations and improved resilience against background interference. This enhanced backbone design directly addresses the core challenge of detecting small-scale and fine-grained defects in transmission line imagery, thereby serving as a crucial cornerstone for the subsequent TinyDef-DETR framework. The overall architecture of the proposed EE-ResNet is illustrated in Fig. 3.

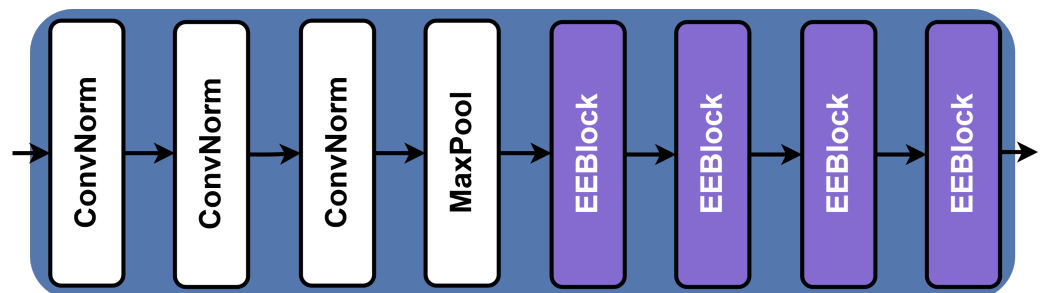


Figure 3. Overall framework of EE-ResNet

3.3. Space-to-depth Convolution

3.3.1. Principle of SPD(Space-to-depth Convolution)

Given the nature of transmission line defect detection—where the dataset is predominantly composed of small objects—preserving fine-grained information, maintaining balanced feature weighting, and performing effective feature representation learning contribute to improving both accuracy and recall [2].

During an extensive review of the literature, we came across the work of Sunkara and Luo [39], who pointed out that conventional CNN architectures exhibit an inherent limitation, namely the use of strided convolution. They emphasized that such designs inevitably lead to the loss of fine-grained information and result in less effective feature representations, which is particularly detrimental for low-resolution images and small object detection. This explains why conventional CNN-based approaches often fail to meet the requirements of small object detection, where the preservation of subtle spatial details is crucial.

Inspired by their findings, we incorporate the SPD(Space-to-depth Convolution) module into our proposed TinyDef-DETR framework. SPD adopts a stride-free downsampling strategy that redistributes pixels along the channel axis instead of discarding them, thereby preserving pixel-level information while reducing spatial resolution. In this way, TinyDef-DETR achieves more effective feature representations, improving both accuracy and recall for transmission line defect detection.

The SPD operation is defined on an input feature map

$$X \in \mathbb{R}^{S \times S \times C},$$

where S denotes the spatial resolution and C is the channel dimension. The goal is to downsample the spatial resolution by a factor of $scale$ while preserving all pixel-level information. Unlike conventional strided convolution that inevitably discards part of the input, SPD achieves lossless downsampling by spatial-to-channel rearrangement. Formally, the output feature map is given by

$$X' \in \mathbb{R}^{\frac{S}{scale} \times \frac{S}{scale} \times (C \cdot scale^2)}.$$

This transformation can be expressed as a structured partitioning of X . Specifically, for each spatial position (u, v) in X' , its corresponding feature vector is constructed by concatenating the values of X sampled from the $scale \times scale$ local neighborhood in the original feature map:

$$X'(u, v, :) = \bigoplus_{i=0}^{scale-1} \bigoplus_{j=0}^{scale-1} X(u \cdot scale + i, v \cdot scale + j, :)$$

where \bigoplus denotes concatenation along the channel dimension. In this way, all pixels from X are preserved in X' , but redistributed from the spatial dimensions into the channel dimension.

After the SPD transformation, the spatial resolution of the feature map is reduced by a factor of $scale$, while all pixel-level information is preserved through spatial-to-channel rearrangement. Consequently, the number of channels increases by a factor of $scale^2$. To further process this rearranged representation, a subsequent convolution layer is applied, which can be formally expressed as

$$X'' = f_{Conv}(X'; \mathbf{W}, \mathbf{b}), \quad X'' \in \mathbb{R}^{\frac{S}{scale} \times \frac{S}{scale} \times C_2},$$

where \mathbf{W} and \mathbf{b} denote the convolutional kernel weights and bias, respectively. This convolution simultaneously fuses information across the expanded channel dimension and adjusts it to the object dimension C_2 . In this way, the operation not only regulates the channel dimensionality but also enhances local feature representation through the structured partitioning.

An illustrative example of the SPDConv operation is presented in Fig. 4.

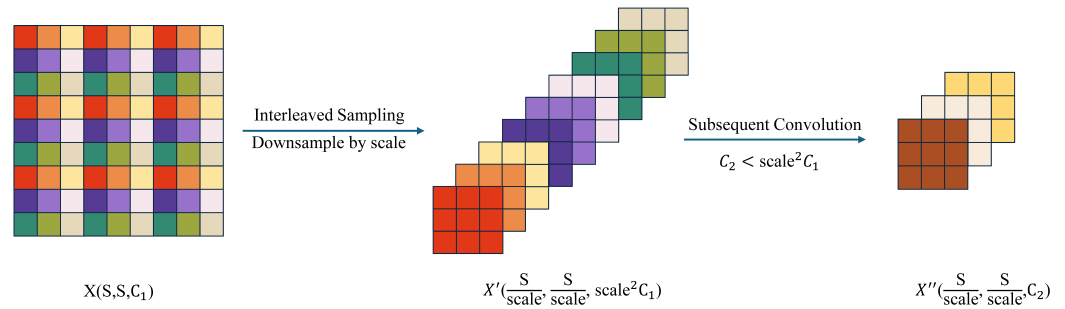


Figure 4. Illustration of SPDConv (Space-to-Depth Convolution)

3.3.2. Choice of the Downsampling Factor

A critical design decision in the SPD module is the choice of the downsampling factor *scale*.

Constraint of Small Object Size. In our dataset, small objects including polluted insulator, missing tie wire, and bird nest frequently span only 8 ~ 32 pixels in the original image. If $scale = 4$ (or larger) were adopted, the smallest objects would be reduced to merely 2 ~ 8 pixels at the first feature level. After further downsampling by the backbone and feature pyramid, these objects would rapidly degenerate into near-point responses, severely hindering recall. By contrast, $scale = 2$ preserves the effective resolution of small objects at the 4 ~ 16 pixel level, which can still be robustly captured and aggregated by local 3×3 operators.

Compatibility with Detector Stride Hierarchy. Unlike many mainstream detectors that organize feature pyramids with strides $\{4, 8, 16, \dots\}$, our Edge Enhanced ResNet employs stage-wise downsampling with $stride = 2$. Consequently, setting SPD $scale = 2$ is equivalent to a lossless stride-2 operation, perfectly aligned with the subsequent stride-2 downsampling in the backbone/pyramid, preserving high-resolution shallow features crucial for small objects. In contrast, starting with $scale = 4$ effectively performs a stride-4 rearrangement at the outset, over-compressing shallow maps and weakening the small-object modeling capacity of early pyramid levels.

Anti-Aliasing and Information Fidelity. With $scale = 2$, the neighborhood is completely mapped into the channel dimension, ensuring that no samples are discarded. Although $scale \geq 4$ also performs rearrangement, the resulting features must be processed at a much lower spatial resolution, reducing the discriminability of local topology and diminishing the effective anti-aliasing capability.

Efficiency in Computation and Memory. After SPD, the channel dimension increases by a factor of $scale^2$. When $scale = 2$, channels are quadrupled while spatial dimensions are reduced by one quarter. As a result, the computational cost of the following 3×3 convolution remains comparable to that of a standard stride-2 convolution, but without discarding information. In contrast, $scale = 4$ would increase the channel dimension by sixteen while reducing spatial size by one sixteenth, leading to heavier memory and bandwidth requirements and potentially unstable training.

Taken together, these factors demonstrate that setting $\text{scale} = 2$ provides the optimal trade-off between recall and efficiency in datasets dominated by small objects, and we therefore adopt it as the fixed parameter in the SPD module of TinyDef-DETR.

3.3.3. Design of the Subsequent Convolution

Following SPD, we adopt a carefully designed convolutional layer to refine the rearranged features. Specifically, we employ a non-strided convolution with a kernel size of 3×3 . This configuration is chosen because the 3×3 kernel provides the minimal receptive field capable of covering the 2×2 local neighborhood that is redistributed during SPD. In contrast, a 1×1 kernel would only perform channel mixing without explicitly modeling cross-partition spatial relationships, which are essential for capturing subtle structural variations in small defects. Larger kernels such as 5×5 would increase computation without offering proportional benefits for objects of the scale encountered in transmission line inspection.

We set the stride to 1 in order to avoid any additional downsampling. Since the primary motivation of SPD is to preserve pixel-level detail while reducing resolution in a lossless manner, further spatial reduction at this stage would counteract the benefits of SPD and degrade the detection of small defects.

In terms of channel configuration, the input dimensionality after SPD expands to four times the original number of channels, consistent with $\text{scale} = 2$. This expansion ensures that all pixel-level information is preserved in the channel space. The output channel dimension is then set to match the base width of the subsequent stage in TinyDef-DETR, ensuring both computational efficiency and stable gradient propagation across the backbone.

3.4. Cross-Stage Dual-Domain Multi-Scale Attention Module

In transmission line defect detection, most objects are small-scale objects such as cracks, rust spots, or insulator damages. These defects often exhibit weak visual saliency and subtle structural variations, making them difficult to distinguish from complex backgrounds like vegetation, sky, or towers. Conventional convolutional networks are inherently constrained by their limited local receptive fields, and simply enlarging the kernel size to capture global context quickly leads to over-parameterization and substantial computational overhead, while also causing oversmoothing and the loss of fine-grained details[40]. Similarly, traditional attention mechanisms that focus solely on either spatial or channel domains fail to provide sufficient enhancement for ambiguous and small-scale objects[41]. Therefore, a more effective mechanism is required to simultaneously preserve detailed structural information, capture global semantic context, and adaptively emphasize defect-related features.

After an extensive literature review, we find that coupling frequency decomposition with attention is particularly effective for tiny, edge-dominated defects in UAV imagery—preserving high-frequency details and suppressing low-frequency clutter that misleads purely spatial attention. Therefore, we propose CSDMAM, which injects learnable frequency gating directly into the attention formation while retaining anisotropic, large-kernel spatial paths tailored to line-shaped defects.

To improve the effectiveness of transmission lines defect detection, we propose the Cross-Stage Dual-Domain Multi-Scale Attention Module (CSDMAM). Given an input feature map $X \in \mathbb{R}^{B \times C \times H \times W}$, a 1×1 convolution is first applied to adjust the channel dimension. The transformed features are then processed in parallel through multiple specialized branches, and their outputs are aggregated via residual summation before being projected by another 1×1 convolution. This design enables the module to capture

diverse feature representations while maintaining computational efficiency. The overall architecture of CSDMAM is illustrated in Figure 5.

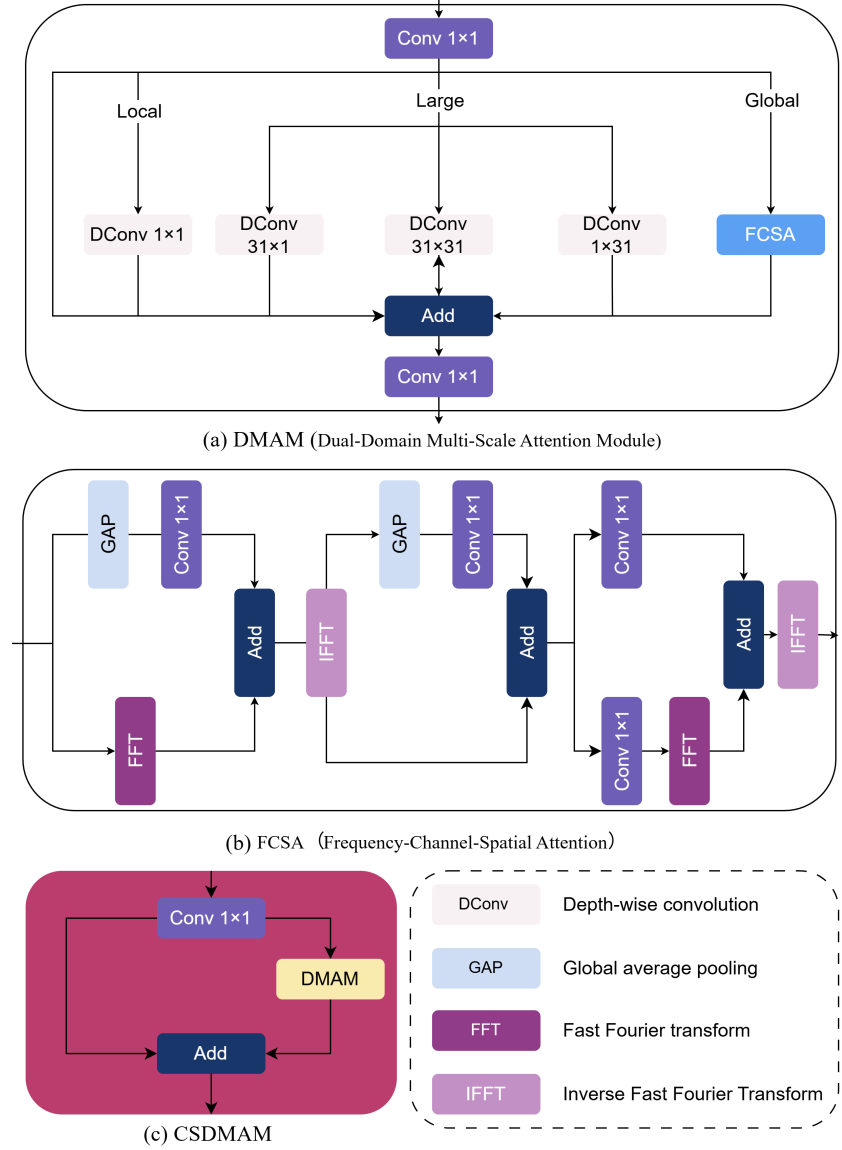


Figure 5. The architecture of the proposed Cross-Stage Dual-Domain Multi-Scale Attention Module (CSDMAM).

To effectively capture complementary information at different scales and semantic levels, CSDMAM is composed of four parallel branches: a Large-Receptive-Field Branch, a Local Detail Preservation Branch, a Global Branch based on the Frequency–Spatial–Channel Attention (FSCA) module, and a Residual Aggregation Branch.

Specifically, to enlarge the receptive field, we add a large-receptive-field branch employing depth-wise convolutions with kernel sizes (k, k) , $(1, k)$, $(k, 1)$, where $k = 31$. The square kernel models global contextual information, while the strip kernels capture elongated dependencies along horizontal and vertical directions, which are especially important for line-shaped structures in transmission infrastructure.

To preserve fine-grained local cues, we further introduce a local branch with a lightweight depth-wise 1×1 convolution, ensuring that subtle defects such as cracks or corrosion spots are not smoothed out by large-kernel operations.

To strengthen semantic discrimination and capture long-range contextual information, we design a Global Branch built upon the Frequency–Spatial–Channel Attention (FSCA)

module, which jointly exploits frequency, spatial, and channel dependencies. Given the input features $X \in \mathbb{R}^{B \times C \times H \times W}$, a two-dimensional Fourier transform is first applied to obtain their frequency-domain representation:

$$X_f = \mathcal{F}(X),$$

where \mathcal{F} denotes the discrete Fourier transform (DFT).

Channel-wise weights are then computed via global average pooling followed by a 1×1 convolution, producing $A_c \in \mathbb{R}^{B \times C \times 1}$. These weights are used to enhance the frequency representation:

$$\tilde{X}_f = A_c \cdot X_f,$$

which is subsequently transformed back into the spatial domain using the inverse DFT:

$$X_{fs} = \mathcal{F}^{-1}(\tilde{X}_f).$$

Next, a spatial-channel reweighting map A_{sc} is generated through global pooling and a 1×1 convolution. This map adaptively emphasizes defect-relevant regions and further refines the feature representation, resulting in the final output of the Global Branch:

$$X_{fscs} = A_{sc} \cdot X_{fs}.$$

To effectively integrate the complementary information captured by all branches, we introduce a residual aggregation branch. In this step, the outputs of the large-receptive-field branch, the local branch, and the FSCA branch are combined with the original input through element-wise summation. This residual fusion mechanism not only preserves the original feature information but also enhances gradient flow and stabilizes training. By consolidating global context, fine-grained details, and dual-domain attention responses into a unified representation, the residual aggregation branch ensures comprehensive feature enhancement and precise defect localization. The final aggregated response is formulated as

$$Y = X + DW_{1,k}(X_n) + DW_{k,1}(X_n) + DW_{k,k}(X_n) + DW_{1,1}(X_n) + X_{fscs},$$

where DW denotes depth-wise convolution with the specified kernel size.

Finally, to further improve computational efficiency and facilitate gradient propagation, we extend the design into a cross-stage structure. Following the Cross Stage Partial (CSP) strategy, the input is split into two parts: one processed by the multi-branch attention module and the other preserved as an identity mapping. The two parts are then concatenated and fused using a 1×1 convolution to produce the final output:

$$Y_{cs} = \text{Conv}\left([\text{DMAM}(X_{\text{branch}}), X_{\text{identity}}]\right).$$

By jointly leveraging large receptive fields, local detail preservation, FSCA-based dual-domain enhancement, and cross-stage fusion, CSDMAM achieves a favorable balance between global semantic understanding and precise defect localization. This design significantly improves the detection of small, visually ambiguous defects in UAV inspection imagery.

3.5. Focaler-Wise-IoU Loss

In transmission-line defect detection, targets are extremely small and exhibit subtle spatial variations, so precise bounding-box regression is pivotal for reliable recognition. IoU-based losses are attractive for their geometric interpretability and optimization efficiency, yet the canonical IoU measures only overlap and provides no informative gradients

when the boxes are disjoint, which stalls learning on difficult examples. Subsequent variants—GIoU [42], DIoU [43], and CIoU [44]—mitigate this to some extent by adding enclosure, center-distance, and aspect-ratio terms. Nevertheless, they still struggle to capture spatial alignment and shape consistency in a unified manner. More advanced designs such as SIoU [45] integrate angular, distance, and shape components, but typically weight all samples uniformly; gradients then become dominated by easy cases while hard, tiny, low-SNR objects receive insufficient emphasis. Focaler-IoU [46] further reshapes the overlap signal by linearly remapping IoU within a fixed interval to favor certain ranges, but its emphasis is uniform and monotonic and it lacks angle-aware distance/shape coupling. Wise-IoU [47] introduces a dynamic, non-monotonic focusing mechanism that suppresses low-quality examples, yet its default formulation is ill-suited to our setting: it deemphasizes geometric shape and aspect consistency that are crucial for sub-pixel localization of tiny defects, it normalizes outlier degree at the batch level—which can miscalibrate under low-SNR, highly imbalanced anchors and inadvertently down-weight informative hard-but-valid samples—and it omits explicit angle-aware distance coupling, yielding weaker guidance for axis-aligned center drift near overlap. Compounding these issues, conventional IoU-based objectives offer limited discrimination in the high-IoU regime where fine-grained localization matters most, leading to slow convergence and reduced accuracy.

To address these shortcomings, we propose Focaler-Wise-SIoU, a unified regression objective that couples normalized IoU scaling, comprehensive geometric penalties, and difficulty-aware modulation. The goal is to sustain strong, stable gradients across the entire overlap spectrum while explicitly promoting spatial alignment and shape fidelity for tiny objects. Concretely, we first introduce a Focaler-IoU overlap surrogate that clips and linearly rescales IoU to sharpen gradients near perfect alignment, while preserving the raw IoU for principled reweighting. We then design SIoU-style geometric penalties that combine an angle-aware, axis-normalized center-distance term with a smooth, saturating shape discrepancy, encouraging accurate alignment and aspect consistency under tiny-object noise. Finally, we incorporate a non-monotonic focal modulation (Wise) driven by an EMA-normalized IoU gap, which highlights informative, moderately hard samples and down-weights both trivial cases and extreme outliers. Raw IoU is used exclusively for difficulty estimation to retain geometric interpretability, and the overall objective remains closed-form, differentiable, and implementation-friendly. These components jointly accelerate convergence and substantially improve localization accuracy on small, low-SNR defects.

The following subsections introduce notation, define each component with its rationale, and present the final loss composition.

3.5.1. Preliminaries and Notation

Let the predicted and target bounding boxes be $B_p = (x_p, y_p, w_p, h_p)$ and $B_t = (x_t, y_t, w_t, h_t)$, parameterized by center coordinates (x, y) and width/height (w, h) . We write the top-left / bottom-right corners as

$$\begin{aligned} x_p^{(1)} &= x_p - \frac{w_p}{2}, & y_p^{(1)} &= y_p - \frac{h_p}{2}, & x_p^{(2)} &= x_p + \frac{w_p}{2}, & y_p^{(2)} &= y_p + \frac{h_p}{2}, \\ x_t^{(1)} &= x_t - \frac{w_t}{2}, & y_t^{(1)} &= y_t - \frac{h_t}{2}, & x_t^{(2)} &= x_t + \frac{w_t}{2}, & y_t^{(2)} &= y_t + \frac{h_t}{2}. \end{aligned}$$

The intersection size is

$$w_{\text{int}} = \max(0, \min(x_p^{(2)}, x_t^{(2)}) - \max(x_p^{(1)}, x_t^{(1)})), \quad (1)$$

$$h_{\text{int}} = \max(0, \min(y_p^{(2)}, y_t^{(2)}) - \max(y_p^{(1)}, y_t^{(1)})). \quad (2)$$

with area $S_{\text{int}} = w_{\text{int}}h_{\text{int}}$. The union area $S_{\text{union}} = w_p h_p + w_t h_t - S_{\text{int}}$, and the standard IoU is

$$\text{IoU} = \frac{S_{\text{int}}}{S_{\text{union}}} \in [0, 1]. \quad (3)$$

We also denote the center displacement by $\Delta = (d_x, d_y) = (x_p - x_t, y_p - y_t)$, and the side lengths of the minimum enclosing rectangle of B_p and B_t by

$$(w_{\text{box}}, h_{\text{box}}) = (\max(x_p^{(2)}, x_t^{(2)}) - \min(x_p^{(1)}, x_t^{(1)}), \max(y_p^{(2)}, y_t^{(2)}) - \min(y_p^{(1)}, y_t^{(1)})). \quad (4)$$

Numerical stability. We use small constants where needed: 10^{-4} in Eq. (7) and $\varepsilon = 10^{-6}$ in Sec. 3.5.6 to avoid singularities; the EMA momentum $m = 10^{-2}$ balances variance and adaptability across training phases.

3.5.2. Focaler-IoU Overlap Term

In transmission-line defect detection most objects are tiny; training benefits from non-saturating gradients even at high overlaps. To strengthen gradient sensitivity near perfect alignment while keeping the geometric meaning of Eq. (3) for reweighting, we use a *clipped and linearly rescaled proxy IoU only* inside the overlap penalty:

$$\text{Io}\hat{\text{U}} = \text{clip}\left(\frac{\text{IoU} - d}{u - d}, 0, 1\right), \quad (d, u) = (0, 0.95), \quad (5)$$

and define

$$L_{\text{IoU}} = 1 - \text{Io}\hat{\text{U}}. \quad (6)$$

High-IoU sensitivity. Using $\text{Io}\hat{\text{U}}$ solely in L_{IoU} preserves gradient magnitude as $\text{IoU} \rightarrow 1$ while the *raw* IoU (Eq. (3)) is retained for difficulty modulation, maintaining geometric interpretability.

3.5.3. Angle-Weighted Distance Penalty (SIoU-style)

Let $\phi \in [0, \pi/4]$ be the acute angle between Δ and its *nearest* coordinate axis:

$$\phi = \arcsin\left(\frac{\min(|d_x|, |d_y|)}{\sqrt{d_x^2 + d_y^2 + 10^{-4}}}\right), \quad (7)$$

where 10^{-4} prevents division by zero when $\Delta \rightarrow 0$. The angle cost in SIoU can be written as $\Lambda = 1 - 2 \sin^2(\phi - \frac{\pi}{4})$. Using $\cos(2\theta) = 1 - 2 \sin^2 \theta$ and $\cos(2\phi - \frac{\pi}{2}) = \sin(2\phi)$, we obtain the exact equivalence

$$\Lambda = \sin(2\phi). \quad (8)$$

We then define

$$\text{Angle} = \sin(2\phi) - 2 = -(2 - \Lambda), \quad (9)$$

so that the distance term below naturally takes the canonical form $1 - \exp((2 - \Lambda) \cdot (\cdot))$: larger misalignment (large $2 - \Lambda$) increases the penalty before purely shrinking the radial offset.

We penalize center offsets per axis with squared, scale-normalized terms:

$$\text{Dist} = 2 - \exp\left(\text{Angle} \cdot \left(\frac{d_x}{w_{\text{box}}}\right)^2\right) - \exp\left(\text{Angle} \cdot \left(\frac{d_y}{h_{\text{box}}}\right)^2\right). \quad (10)$$

Because $\text{Angle} \leq 0$ by Eq. (9), each exponential factor decreases as the (normalized) offset grows, hence Dist is monotone in misalignment while remaining smooth around zero.

Axis-wise normalization ensures scale invariance across object sizes, contributing to the overall *scale invariance* of the loss.

3.5.4. Shape Consistency Penalty

Tiny defects often suffer from annotation noise; a saturating yet smooth transform mitigates the dominance of extremely large aspect errors while keeping sensitivity to moderate mismatches. We adopt

$$\text{Shape} = \left(1 - \exp\left(-\frac{|w_p - w_t|}{\max(w_p, w_t)}\right)\right)^\theta + \left(1 - \exp\left(-\frac{|h_p - h_t|}{\max(h_p, h_t)}\right)\right)^\theta, \quad \theta = 4. \quad (11)$$

For small relative deviations, $1 - \exp(-x) \approx x$ is near-linear; for large deviations it saturates towards 1, and the exponent θ further curbs outliers while preserving gradients for mid-range shape errors. This saturating design improves *robustness to annotation noise* on tiny objects without letting large, noisy deviations dominate the loss.

3.5.5. Geometric Core: Overlap + Alignment + Shape

Combining the overlap penalty (Eq. (6)) with the distance and shape terms (Eqs. (10)–(11)), we obtain the SIoU-style geometric core:

$$L_{\text{SIoU}} = L_{\text{IoU}} + \frac{1}{2}(\text{Dist} + \text{Shape}). \quad (12)$$

The factor 1/2 balances alignment/shape against overlap so that none dominates the gradient field in typical training regimes. Note again that only L_{IoU} uses the rescaled $\hat{\text{IoU}}$; all reweighting below relies on the *raw* IoU.

3.5.6. Wise Difficulty Modulation via EMA Normalization

We quantify sample difficulty with the normalized IoU gap

$$\beta = \frac{1 - \text{IoU}}{\mathbb{E}[1 - \text{IoU}]}, \quad \mathbb{E}[1 - \text{IoU}] \leftarrow (1 - m) \mathbb{E}[1 - \text{IoU}] + m \cdot (1 - \text{IoU})_{\text{batch}}, \quad (13)$$

where the expectation is tracked by an exponential moving average (EMA). We use $m = 10^{-2}$, which is stable yet responsive for shifts across training phases; in practice we add a tiny $\varepsilon = 10^{-6}$ to the denominator for numerical stability. Crucially, Eq. (13) operates on the *raw* IoU from Eq. (3) to preserve geometric interpretability.

To emphasize moderately hard examples while avoiding overfitting to extreme outliers, we employ the following modulation:

$$\gamma(\beta) = \frac{\beta}{\delta \alpha^{(\beta - \delta)}}, \quad \alpha = 1.7, \delta = 2.7. \quad (14)$$

This non-monotonic weighting targets *informative* moderately hard samples around $\beta \approx \delta$, gently down-weights trivially easy cases ($\beta \ll \delta$) and prevents domination by extreme outliers as $\beta \gg \delta$.

3.5.7. Final Objective and Batch-wise Computation

Multiplying the geometric core (Eq. (12)) by the difficulty weight (Eq. (14)) yields the *Focaler-Wise-SIoU* objective:

$$L = \left(1 - \hat{\text{IoU}} + \frac{1}{2}(\text{Dist} + \text{Shape})\right) \cdot \gamma(\beta), \quad \beta = \frac{1 - \text{IoU}}{\mathbb{E}[1 - \text{IoU}]} \quad (15)$$

We now detail a concise batch-wise procedure that operationalizes Eqs. (5)–(11) and (13)–(14) into a practical training routine:

Algorithm 1 Per-mini-batch computation of Focaler-Wise-SIoU

- Require:** predictions B_p , targets B_t ; running mean $\mu = \mathbb{E}[1 - \text{IoU}]$; hyperparameters $(d, u) = (0, 0.95)$, $m = 10^{-2}$, $\theta = 4$, $(\alpha, \delta) = (1.7, 2.7)$; $\varepsilon = 10^{-6}$
- 1: **Raw/Proxy IoU:** compute raw IoU (Eq. (3)); compute IoU (Eq. (5)); set $L_{\text{IoU}} = 1 - \hat{\text{IoU}}$ (Eq. (6))
 - 2: **Distance geometry:** compute ϕ (Eq. (7)), Angle (Eq. (9)), $w_{\text{box}}, h_{\text{box}}$ (Eq. (4)); then Dist (Eq. (10))
 - 3: **Shape:** compute Shape (Eq. (11)) with θ
 - 4: **Core loss:** $L_{\text{SIoU}} \leftarrow L_{\text{IoU}} + \frac{1}{2}(\text{Dist} + \text{Shape})$ (Eq. (12))
 - 5: **Difficulty (raw IoU):** $\beta \leftarrow (1 - \text{IoU})/(\mu + \varepsilon)$ (Eq. (13)); $w \leftarrow \gamma(\beta) = \beta/(\delta \alpha^{(\beta-\delta)})$ (Eq. (14))
 - 6: **Aggregate:** $L \leftarrow \text{mean}(L_{\text{SIoU}} \cdot w)$ over positive matches (Eq. (15))
 - 7: **EMA update:** $\mu \leftarrow (1 - m)\mu + m \cdot \text{mean}(1 - \text{IoU})$ (Eq. (13))
-

4. Experiments and Results Analysis

4.1. Datasets

In this paper, we use the CSG-ADCD dataset. The CSG-ADCD (China Southern Grid Aerial Defective Component Dataset) is a large-scale, high-resolution UAV-based image dataset specifically developed for the detection of defects in power transmission line components, including insulators, tie wires, and poles. Constructed under authentic inspection scenarios by China Southern Power Grid, the dataset comprises 10,000 aerial images. Each image was manually annotated by a single domain expert to ensure both consistency and high-quality labeling.

In total, the dataset contains 73,448 annotated instances covering nine component states or defect types: Normal Insulator (zcjyz), Polluted Insulator (jyzwh), Damaged Pole (dgss), Missing Tie Wire (zxqs), Loose Tie Wire (zxst), Insulator Flashover (jyzsl), Bird Nest (nw), Broken Insulator (jyzps), and Shattered Post Insulator (zyzsl).

Table 1 provides a correspondence between the labels and category names for each defect type in the dataset, offering a clear overview of the classification scheme used.

On average, each object occupies a pixel area of 422.12, with the dataset exhibiting a highly imbalanced distribution in terms of object sizes: 94.51% small objects (69,413 instances), 5.48% medium-sized (4,022 instances), and only 0.02% large (13 instances). This reflects the intrinsic characteristics of UAV-based transmission line inspection objects, which are often small, localized, and partially occluded.

For training consistency, all images were preprocessed by resizing the longer side to 640 pixels while preserving aspect ratio, followed by padding to a fixed resolution of 640 × 640 pixels using gray borders. The dataset is split into 8,000 training, 1,000 validation, and 1,000 test images.

Statistical analysis further highlights two key features of the dataset. First, the scatter distribution of object width and height reveals a strong concentration of samples in the lower-left region, confirming the overwhelming dominance of small-scale objects. Second, the number of objects per image follows a relatively stable distribution, averaging 7.34 instances per image, with 2,285 images containing between 7 and 8 objects. This regularity is particularly beneficial for developing models optimized for dense and small-object detection.

In summary, the CSG-ADCD dataset demonstrates strong representativeness by simultaneously addressing two critical aspects. On the one hand, it captures a comprehensive range of component defects and status indicators that are directly relevant to transmission

Table 1. Correspondence between labels and category names

No.	Label	Name
1	zcjyz	Normal Insulator
2	jyzwh	Polluted Insulator
3	dgss	Damaged Pole
4	zxqs	Missing Tie Wire
5	zxst	Loose Tie Wire
6	jyzsl	Insulator Flashover
7	nw	Bird Nest
8	jyzps	Broken Insulator
9	zyzsl	Shattered Post Insulator

safety, while also reflecting the complexity of real-world inspection conditions such as occlusion, cluttered backgrounds, and varying illumination. On the other hand, its pronounced dominance of small-scale objects—over 94% of all annotated instances—together with the presence of subtle and fine-grained anomalies, makes it a highly challenging and domain-specific benchmark. In this regard, CSG-ADCD not only advances research in defect detection for power systems but also provides a valuable testbed for generic small-object detection in aerial remote sensing, offering greater domain relevance than existing datasets such as VisDrone[48].

Overall, CSG-ADCD constitutes a robust and high-fidelity benchmark, offering significant value for advancing research in both domain-specific defect detection and general small-object detection tasks.

As shown in Fig.6, the vast majority of objects are smaller than 32×32 pixels, placing them within the small-object category. The scatter plot depicts the distribution of annotated instances by pixel width and height after preprocessing, with different categories distinguished by distinct colors in the legend. The strong concentration of points in the lower-left corner highlights the predominance of small and compact objects, consistent with the characteristics of transmission-line inspection imagery. Dashed reference lines at 32×32 and 96×96 pixels mark the boundaries between small, medium, and large regimes, clearly revealing the relative scarcity of medium- and large-sized objects.

Overall, the visualization emphasizes the dominance of small instances and underscores the dense, fine-grained nature of aerially captured transmission-line defects.

4.2. Model Training and Evaluation Metrics

We implement the proposed model on the PyTorch framework and build it upon the Ultralytics RT-DETR backbone initialized with pretrained weights. Training is conducted on a workstation with an NVIDIA GeForce RTX 3090 (24 GB) running Ubuntu 20.04, Python 3.10.14, PyTorch 2.3.1, and CUDA 12.1. The model is trained for 100 epochs with a batch size of 4 and an input resolution of 640×640 , using AdamW with an initial learning rate 1.0×10^{-4} , a final learning-rate factor $lrf = 1.0$, momentum 0.9, and weight decay 1.0×10^{-4} . We apply a 2000-iteration warm-up with momentum set to 0.8 and a bias learning rate of 0.1.

Validation follows the COCO protocol on the validation split: we report mAP_{50} (AP at $IoU = 0.50$) and $mAP_{50:95}$ (AP averaged over IoU thresholds from 0.50 to 0.95 in steps of 0.05). Inference uses class-agnostic non-maximum suppression with an IoU threshold of 0.7 and at most 300 detections per image; this IoU is unrelated to the evaluation thresholds.

In the task of UAV-based power transmission line defect detection, the performance of different detection algorithms may vary significantly under diverse operational scenarios.

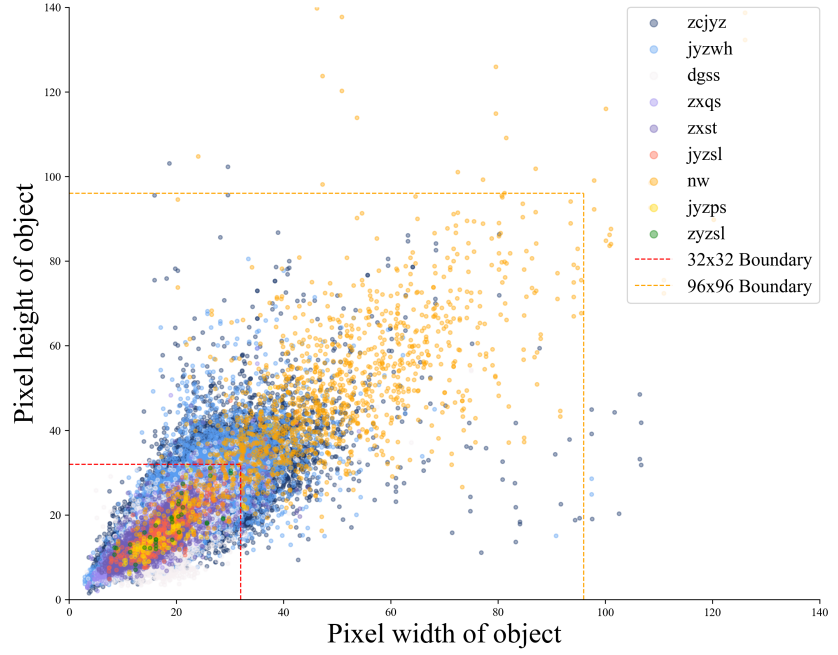


Figure 6. Distribution of object sizes in CSG-ADCD

The inference capability of a detection model is typically evaluated using several criteria, including: the computational complexity measured in floating-point operations (FLOPs), and a series of key performance metrics such as precision (P), recall (R), average precision (AP), and mean average precision (mAP). These metrics are formally defined as follows:

$$P = \frac{TP}{TP + FP}$$

Precision (P) measures the proportion of correctly detected defect instances among all predicted defect instances. A higher precision indicates that the model produces fewer false alarms (false positives), which is critical for avoiding unnecessary inspection or maintenance actions.

$$R = \frac{TP}{TP + FN}$$

Recall (R) reflects the proportion of correctly detected defect instances among all actual defect instances. A higher recall indicates that the model misses fewer true defects (false negatives), which is essential for ensuring the completeness of defect identification in safety-critical applications.

$$AP = \int_0^1 P(R) dR$$

The average precision (AP) is computed as the area under the precision–recall curve. It captures the trade-off between precision and recall across different confidence thresholds, providing a more comprehensive evaluation of the detection performance for a single defect category.

$$mAP = \frac{1}{k} \sum_{i=1}^k AP_i$$

The mean average precision (mAP) represents the mean value of AP over k defect categories. It is widely recognized as the most comprehensive metric for evaluating

detection models, as it jointly considers both detection accuracy and robustness across multiple defect types.

In addition to these general measures, the COCO evaluation protocol further defines scale-sensitive metrics, such as: AP_s and AP_m , to provide deeper insights into detection performance across different object sizes. Specifically, AP_s evaluates the average precision for small objects (with areas less than 32^2 pixels), while AP_m measures the average precision for medium-sized objects (with areas between 32^2 and 96^2 pixels). Since the majority of defects in transmission line inspection datasets are small in scale, AP_s serves as a particularly critical indicator, directly reflecting the model’s capability to capture subtle and fine-grained defect patterns that occupy only a limited number of pixels. Therefore, the COCO metrics AP_s and AP_m are employed in this study to assess detection performance across different object scales.

Here, TP (true positives) denotes the number of correctly detected defect instances, FP (false positives) refers to non-defect regions mistakenly identified as defects, FN (false negatives) indicates defect regions that were not detected, and k denotes the total number of defect categories. Together, these metrics provide a balanced overall performance in terms of accuracy, completeness, and overall reliability, which is important for real-time transmission line inspection tasks.

4.3. Comparison of heatmaps

To intuitively demonstrate the effectiveness of the proposed modules, we generate heatmaps from the baseline RT-DETR model and the model with the proposed modules (EE-ResNet, SPD Convolution, and CSDMAM) on the same input image. These heatmaps illustrate the attention distribution of the models during the recognition process. As shown in Fig.7, subfigures (a), (c), and (e) represent the attention maps from the baseline model corresponding to the modules before integration, while subfigures (b), (d), and (f) show the attention maps after incorporating the proposed modules. It can be observed that the attention distribution after the inclusion of the modules is more fine-grained, and the object contours are more distinct, indicating that the proposed modules enhance the model’s ability to preserve more detailed information.

4.4. Ablation Study of the Proposed Method

To analyze the impact of each component in CSG-ADCD, we conduct ablation studies by selectively enabling and disabling four key modules: EER (Edge-Enhanced ResNet), SPD (Stride-free Space-to-Depth), CSDMAM (Cross-Stage Dual-Domain Multi-Scale Attention Module), and FWS Loss (Focaler-Wise-SIoU Loss). The results in Table 2 quantify each module’s contribution across multiple evaluation metrics. Here, \checkmark denotes an enabled module, and \times denotes a disabled one.

Table 2. Ablation Experiments for CSG-ADCD

<i>EER</i>	<i>SPD</i>	<i>CSDMAM</i>	<i>FWSLoss</i>	GFLOPs	Precision	Recall	mAP ₅₀	AP _s
\times	\times	\times	\times	57.0	0.369	0.177	0.163	0.071
\checkmark	\times	\times	\times	57.0	0.444	0.203	0.189	0.073
\times	\checkmark	\times	\times	59.9	0.486	0.195	0.190	0.083
\times	\times	\checkmark	\times	72.8	0.458	0.166	0.165	0.072
\times	\times	\times	\checkmark	57.0	0.500	0.204	0.207	0.082
\checkmark	\checkmark	\times	\times	59.7	0.417	0.208	0.192	0.076
\checkmark	\times	\checkmark	\times	66.0	0.425	0.190	0.189	0.077
\times	\checkmark	\checkmark	\times	65.2	0.385	0.192	0.182	0.072
\checkmark	\checkmark	\checkmark	\times	65.3	0.485	0.233	0.237	0.119
\checkmark	\checkmark	\checkmark	\checkmark	65.3	0.534	0.263	0.275	0.106

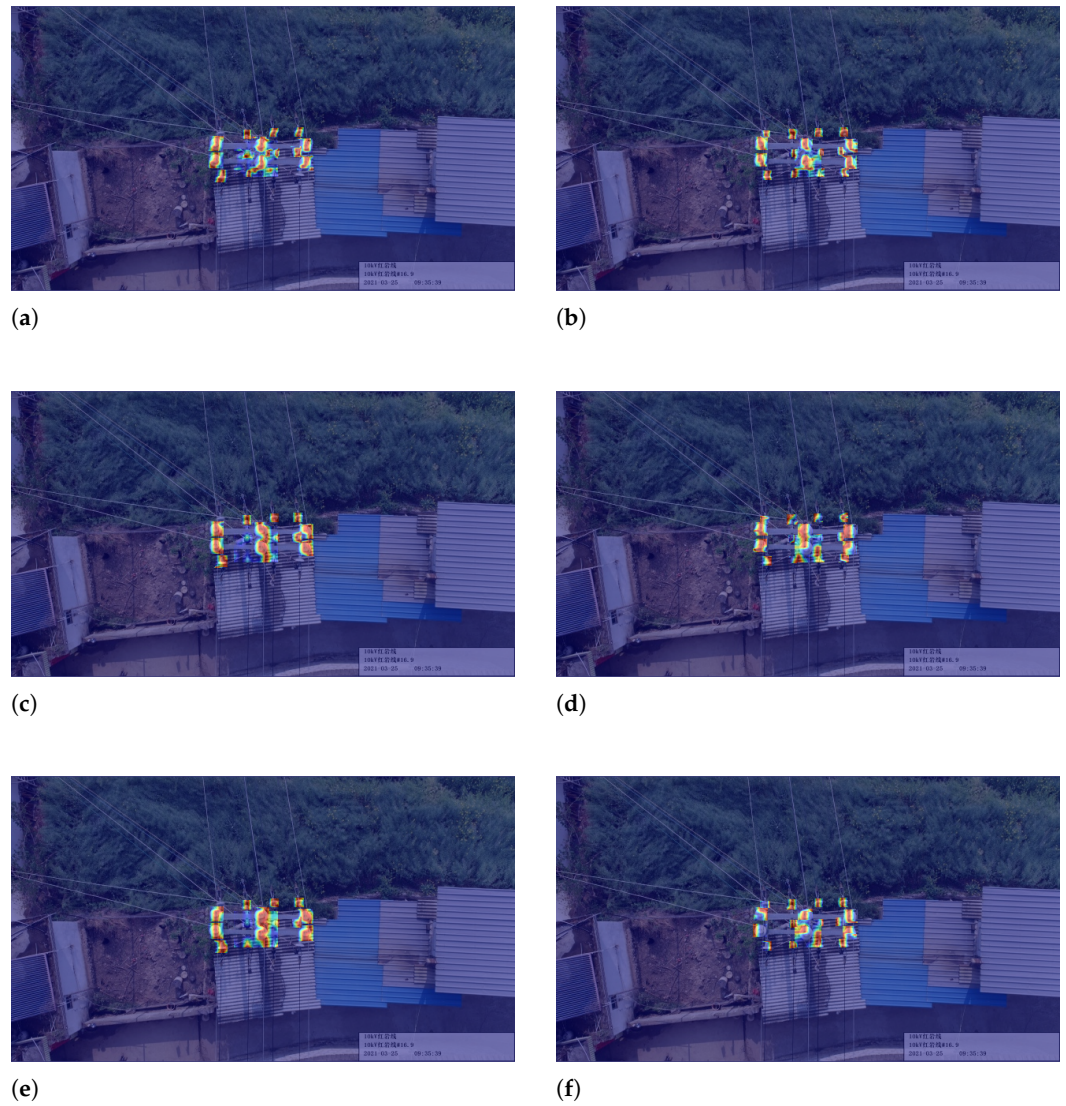


Figure 7. Comparison of attention maps for the baseline RT-DETR model before and after incorporating different innovative modules: (a) without EEBlock, (b) with EEBlock, (c) without SPD Convolution, (d) with SPD Convolution, (e) without CSDMAM, (f) with CSDMAM.

Edge-Enhanced ResNet (EER) EER strengthens boundary-aware features and reduces background leakage. Relative to the bare baseline, precision increases from 0.369 to 0.444, recall rises from 0.177 to 0.203, and mAP_{50} improves from 0.163 to 0.189 at an unchanged 57.0 GFLOPs. These shifts indicate fewer false positives at a fixed confidence threshold and more true positives on low-contrast contours. Importantly for the perceived instability, EER conditions the feature space so that subsequent attention behaves reliably. When EER is combined with SPD and CSDMAM, recall increases further to 0.233 and AP_s for small objects increases from 0.083 with SPD alone to 0.119 with all three. This pattern shows that EER anchors CSDMAM to genuine defect boundaries, turning a potentially volatile attention stage into a consistent contributor to small-object localization.

Space-to-Depth Convolution (SPD) Applied alone, SPD preserves fine spatial evidence while avoiding aliasing, which suppresses spurious activations. Precision increases from 0.369 to 0.486, recall holds near 0.195, and mAP_{50} stays around 0.190, with GFLOPs rising modestly from 57.0 to 59.9. When SPD is paired with EER but without attention, recall increases from 0.195 to 0.208 and mAP_{50} nudges from 0.190 to 0.192, while precision softens from 0.486 to 0.417, which is expected because stronger edge cues surface more borderline candidates before a selective mechanism filters them. Once CSDMAM is added, those candidates are better gated: precision recovers from 0.417 to 0.485 and recall increases from 0.208 to 0.233. Thus, SPD and EER jointly deliver detail-rich, edge-faithful inputs that convert CSDMAM from a possible source of volatility into a consistent enhancer of small-object detection, as reflected by AP_s increasing from 0.083 to 0.119 when all three are enabled.

Cross-Stage Dual-Domain Multi-Scale Attention Module (CSDMAM) The single-module ablation clarifies why a reviewer might perceive instability if attention is used in isolation. Enabling CSDMAM alone increases compute from 57.0 to 72.8 GFLOPs yet does not improve end-to-end accuracy: precision moves from 0.369 to 0.458, recall decreases from 0.177 to 0.166, and mAP_{50} remains near baseline at 0.165. This outcome indicates that, without edge priors or detail-preserving downsampling, attention can over-weight textured background regions and depress recall. Pairwise ablations corroborate this dependency: adding CSDMAM to SPD reduces precision from 0.486 to 0.385, and adding it to EER lowers precision from 0.444 to 0.425. In contrast, when CSDMAM is combined with both EER and SPD, its intended role materializes: mAP_{50} increases from 0.190 with SPD alone to 0.237 with all three modules, and AP_s for small objects increases from 0.083 to 0.119. Hence, CSDMAM is not intrinsically unstable; it becomes reliably beneficial once the backbone provides clean edges and SPD preserves the fine-scale evidence that attention needs to gate.

Focaler-Wise-SIoU Loss (FWS Loss) FWS Loss converts representational gains into better calibration and tighter alignment. When applied to the EER–SPD–CSDMAM stack, precision increases from 0.485 to 0.534, recall increases from 0.233 to 0.263, and mAP_{50} increases from 0.237 to 0.275. These simultaneous gains show improved confidence shaping and stricter localization. Two interactions clarify the trade-offs. First, relative to the bare baseline, AP_s for small objects increases from 0.071 to 0.106 under the full configuration, confirming stronger tiny-target localization on average. Second, relative to the three-module model without the loss, AP_s decreases from 0.119 to 0.106 even as global metrics improve. This pattern reflects FWS Loss emphasizing medium-difficulty samples and penalizing loose boxes, which can prune marginal small-object detections at the chosen thresholds. In practice, this behavior is tunable by slightly relaxing the classification prior for the smallest anchors or moderating the modulation strength in the loss. Overall, FWS Loss interacts constructively with EER, SPD, and CSDMAM—stabilizing predictions, curbing over-confident false positives, and reinforcing the complementary effects of the modules—thereby addressing the instability observation within a co-designed pipeline.

4.5. Comparisons With Previous Methods

In this section, we conduct a rigorous comparative study between the proposed TinyDef-DETR and representative state-of-the-art detectors spanning one-stage (e.g., YOLOv5/8/10/11), two-stage/cascade paradigms, and Transformer-based frameworks (e.g., RT-DETR, Conditional-DETR, DINO). All models are evaluated under a unified protocol—identical data splits, input resolution, and training hyperparameters—to ensure fairness.

Before presenting the experimental data, to visually highlight the differences between TinyDef-DETR and other representative detectors, we conduct a case study on four representative images from the CSG-ADCD dataset. To save space and facilitate readability in a scenario where the majority of objects are small objects, we render the detection bounding boxes with filled colors rather than outlines only. This visualization provides a clearer comparison of recognition results across different models, and the detection results are illustrated in Fig. 8.

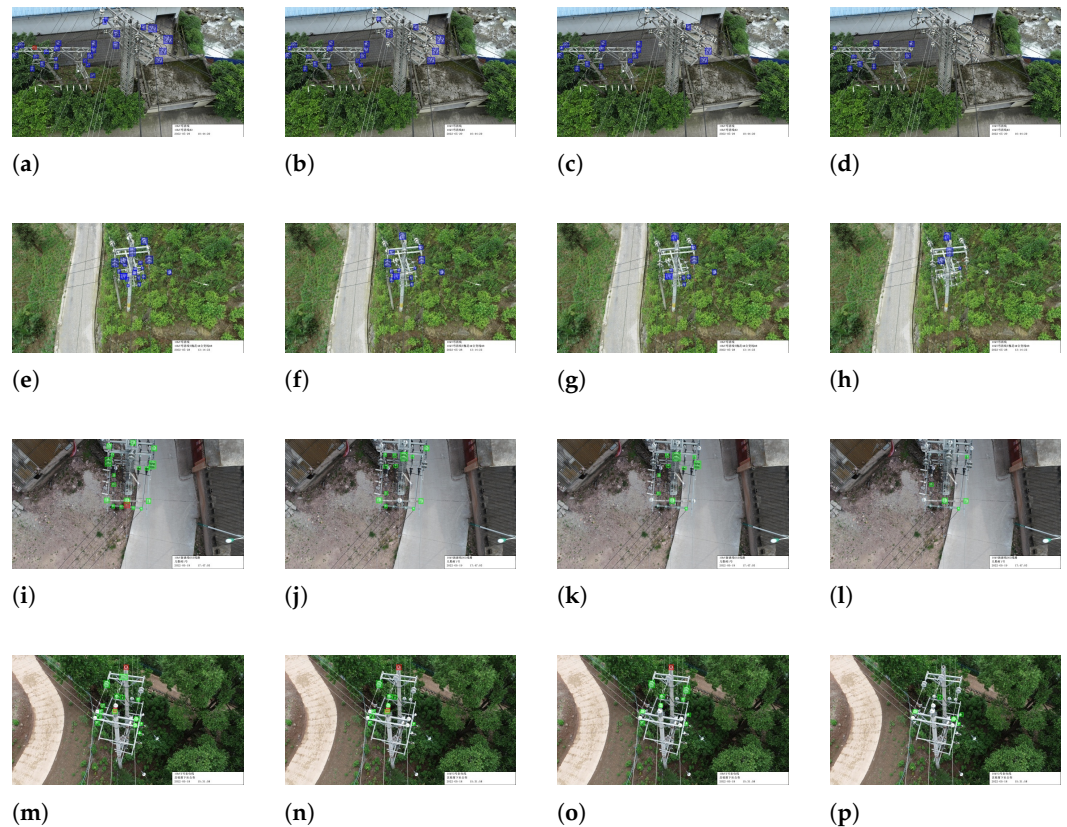


Figure 8. Comparison of detection results from four object detection methods on four representative test samples. Rows (a)–(d) correspond to different test images, and the four columns show the results obtained by TinyDef-DETR, DINO, RT-DETR-R18, and YOLO v5s, respectively.

Table 3 summarizes the overall performance of representative detectors on the CSG-ADCD dataset. The comparison covers lightweight and standard variants of YOLO (v5, v8, 10, 11), Transformer-based models such as RT-DETR and Conditional-DETR, as well as classical baselines including RetinaNet and DETR. Key indicators, including the number of parameters, computational complexity (GFLOPs), Precision, Recall, mAP_{50} , and $mAP_{50:95}$, are reported to provide a comprehensive view of accuracy–efficiency trade-offs. The best values in each column are highlighted in bold for clarity.

For a fair comparison, all methods are evaluated under a unified protocol—an input resolution of 640×640 , identical NMS settings, and the same maximum number of detections per image.

In addition, part of the models are implemented with MMDetection, an open-source object detection toolbox based on PyTorch, which is a core component of the OpenMMLab [49] project. This ensures standardized training pipelines, reproducibility, and fair comparison across different architectures.

It is also worth noting that DINO[11]—evaluated under *identical hardware and software* using the official OpenMMLab [49] recipe `dino-4scale_r50_8xb2-12e_coco` with its default 12-epoch schedule—performs worse than TinyDef-DETR across all reported metrics, while requiring **79.8 hours** of training; by contrast, TinyDef-DETR, trained with our default 100-epoch schedule on the same setup, completes in **under 20 hours**. Although wall-clock time is environment-dependent, these figures reflect realistic, recommended settings, and TinyDef-DETR thus offers a more favorable accuracy–efficiency trade-off for real-world UAV inspection—amusingly, it seems this “longer training, better performance” effect doesn’t always make sense.

To further highlight performance on small objects and defect-specific categories, Table 4 reports additional evaluation metrics. These include Recall and mAP_{50} for Polluted Insulator (jyzwh) and Damaged Pole (dgss), which are the two most frequently occurring defect types in transmission line inspection scenarios and are therefore selected as representative categories for detailed evaluation, alongside scale-sensitive measures AP_s and AP_m . Such results enable a fine-grained comparison of detection performance.

Table 3. Model Performance Evaluation: Precision, Recall, and mAP for CSG-ADCD

Model	Parameters (M)	GFLOPs	Precision	Recall	mAP_{50}	$mAP_{50:95}$
YOLO v5n	2.2	5.8	0.707	0.131	0.131	0.0628
YOLO v5s	9.1	23.8	0.346	0.148	0.140	0.0646
YOLO v5m	25.1	64.0	0.548	0.164	0.162	0.0717
YOLO v8n	2.7	6.8	0.580	0.134	0.133	0.0613
YOLO v8s	11.1	28.5	0.375	0.155	0.147	0.0661
YOLO v8m	23.2	67.5	0.403	0.169	0.163	0.0719
YOLO 10n[50]	2.7	8.2	0.707	0.125	0.133	0.0627
YOLO 10s	8.0	24.5	0.536	0.144	0.157	0.0725
YOLO 10m	16.6	63.5	0.386	0.170	0.162	0.0753
YOLO 11n[51]	2.6	6.3	0.638	0.135	0.136	0.0641
YOLO 11s	9.4	21.3	0.516	0.166	0.155	0.0717
YOLO 11m	20.0	67.7	0.399	0.181	0.173	0.0776
RT-DETR-l	32.8	108.0	0.480	0.189	0.199	0.0890
RT-DETR-x	65.5	222.5	0.485	0.199	0.216	0.0990
RT-DETR-R18	19.8	57.0	0.369	0.177	0.163	0.0738
RT-DETR-R34	31.2	88.8	0.354	0.127	0.117	0.0533
RT-DETR-R50	42.9	134.8	0.363	0.120	0.115	0.0514
RT-DETR-R101	74.7	247.1	0.467	0.185	0.193	0.0879
Conditional-DETR-R18[52]	–	–	0.309	0.068	0.038	0.0110
Conditional-DETR-R34	–	–	0.447	0.082	0.034	0.0090
Conditional-DETR-R50	44.0	89.5	0.568	0.159	0.172	0.0660
DETR-R50[53]	–	–	0.301	0.138	0.124	0.0430
RetinaNet[54]	12.0	33.8	0.394	0.029	0.013	0.0040
DINO[11]	–	–	0.496	0.257	0.224	0.0986
FFCA-YOLO[55]	7.1	51.4	0.680	0.130	0.142	0.0596
TinyDef-DETR	20.5	65.3	0.534	0.263	0.275	0.1187

A comprehensive illustration of the trade-off between detection accuracy and computational efficiency is presented in Fig. 9, where the results reported in Table 3 are visualized. The plot highlights the relative positions of different detectors in terms of mAP_{50} ver-

sus GFLOPs, enabling an intuitive comparison of the accuracy–efficiency balance across lightweight YOLO variants, Transformer-based detectors, and the proposed TinyDef-DETR. Notably, TinyDef-DETR achieves an mAP_{50} of 0.275 with a computational cost of only 65.3 GFLOPs, striking a favorable balance between accuracy and efficiency compared with both lightweight YOLO models and heavier Transformer-based detectors.

Furthermore, Table 4 provides a more detailed view of performance on small objects and defect-specific categories. It reports Recall and mAP_{50} for Polluted Insulator (jyzwh) and Damaged Pole (dgss) — the two most frequently occurring defect types in transmission line inspection — alongside scale-sensitive metrics AP_s and AP_m . These results offer deeper insights into model behavior and enable fine-grained performance comparisons across representative defect categories.

Finally, a holistic comparison of the selected detectors is presented in the form of a radar chart (Fig. 10). The models included — YOLO v5m, YOLO v8m, YOLO 11m, RT-DETR-R18, RT-DETR-x, and TinyDef-DETR — represent both one-stage and Transformer-based detection paradigms. The evaluation encompasses a comprehensive set of indicators, namely Recall, mAP_{50} , $mAP_{50:95}$, AP_s , AP_m , Recall of Polluted Insulator (jyzwh), mAP_{50} of Polluted Insulator, and mAP_{50} of Damaged Pole (dgss). For enhanced visual comparability, each metric is normalized to its maximum value.

4.6. Generalization Experiments for the Proposed Methods

Since small objects dominate our dataset, we further evaluate the proposed method on the VisDrone-DET 2019 benchmark, a widely used UAV dataset for object detection in images. VisDrone-DET 2019[48] comprises 8,599 drone-captured images with >540k annotated bounding boxes across 10 general-purpose categories (e.g., pedestrian, person, car, van, bus, truck, motor, bicycle, awning-tricycle, tricycle), split into 6,471/548/1,580 for train/val/test. Importantly, VisDrone does not include transmission-line defect classes. Therefore, our results on VisDrone (Table 5) assess cross-domain transferability rather than in-domain recognition. Owing to its dense object distribution, the high proportion of small targets, and complex real-world conditions, VisDrone provides a rigorous testbed for robustness and generalization. The strong performance we observe thus demonstrates our framework’s general efficacy for small-object detection in UAV imagery, beyond the specific domain of transmission-line inspection, which is practically valuable.

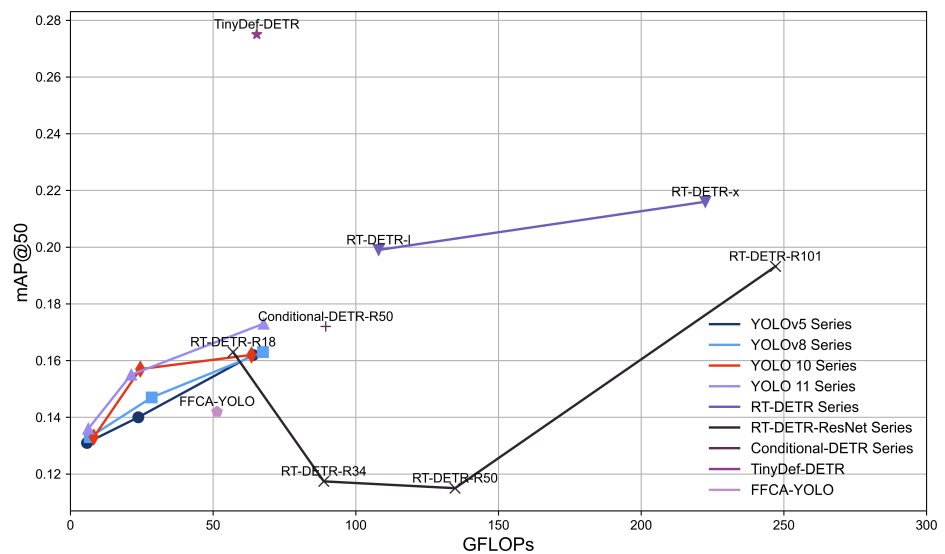


Figure 9. Comparison of model performance in terms of mAP_{50} versus GFLOPs. For clarity and to save space, labels for YOLO series are omitted; within each series, the models are ordered by GFLOPs from left to right as n, s, and m.

Table 4. Model Performance Metrics: Recall, mAP50, AP_s, and AP_m for jyzwh and dgss

Model	Recall (jyzwh)	mAP ₅₀ (jyzwh)	mAP ₅₀ (dgss)	AP _s	AP _m
YOLO v5n	0.352	0.315	0.258	0.061	0.097
YOLO v5s	0.377	0.314	0.270	0.065	0.098
YOLO v5m	0.372	0.367	0.277	0.079	0.081
YOLO v8n	0.364	0.321	0.264	0.066	0.078
YOLO v8s	0.388	0.331	0.269	0.067	0.095
YOLO v8m	0.378	0.360	0.296	0.075	0.087
YOLO 10n[50]	0.352	0.321	0.251	0.062	0.094
YOLO 10s	0.343	0.341	0.308	0.078	0.095
YOLO 10m	0.390	0.356	0.294	0.075	0.097
YOLO 11n[51]	0.353	0.324	0.245	0.060	0.103
YOLO 11s	0.381	0.344	0.291	0.074	0.100
YOLO 11m	0.382	0.373	0.307	0.082	0.094
RT-DETR-l	0.360	0.341	0.372	0.078	0.044
RT-DETR-x	0.366	0.363	0.403	0.083	0.058
RT-DETR-R18	0.347	0.316	0.354	0.071	0.039
RT-DETR-R34	0.293	0.260	0.284	0.056	0.062
RT-DETR-R50	0.278	0.254	0.275	0.054	0.027
RT-DETR-R101	0.345	0.316	0.378	0.073	0.050
Conditional-DETR-R18[56]	0.150	0.073	0.082	0.009	0.016
Conditional-DETR-R34	0.184	0.063	0.059	0.006	0.011
Conditional-DETR-R50	0.406	0.389	0.287	0.064	0.057
DETR-R50[53]	0.289	0.280	0.203	0.041	0.037
RetinaNet[54]	0.048	0.022	0.006	0.012	0.003
FFCA-YOLO[55]	0.286	0.291	0.270	0.059	0.051
TinyDef-DETR	0.397	0.391	0.419	0.106	0.110

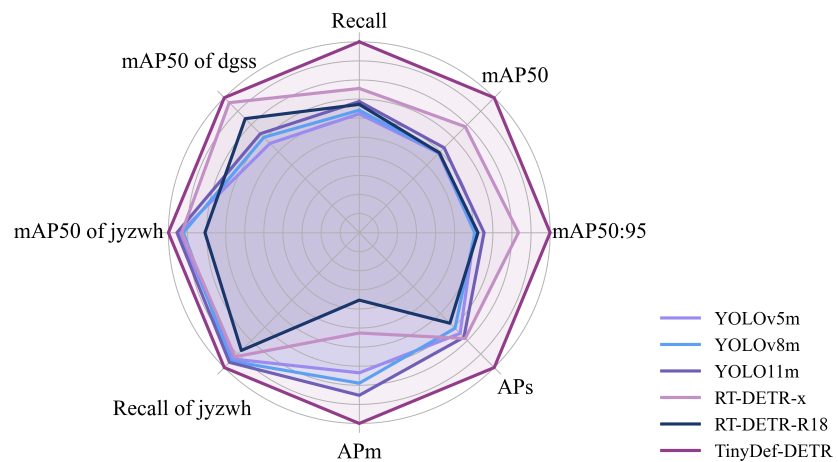
**Figure 10.** Radar Chart of Performance Comparison on Transmission Line Defect Detection

Table 5. Comparison Experiments for TinyDef-DETR on VisDrone

Model	Param(M)	GFLOPs	mAP ₅₀	mAP _{50:95}	AP _s	AP _m
YOLO v8n	3.0	8.1	0.259	0.144	0.059	0.225
YOLO v8s	11.1	28.5	0.307	0.173	0.078	0.269
YOLO v8m	25.9	78.7	0.332	0.190	0.090	0.294
YOLO 10n[50]	2.3	6.5	0.261	0.142	0.063	0.224
YOLO 10s	7.2	21.4	0.323	0.179	0.086	0.278
YOLO 10m	15.3	58.9	0.345	0.195	0.097	0.300
YOLO 11n[51]	2.6	6.3	0.258	0.142	0.058	0.225
YOLO 11s	9.4	21.3	0.313	0.176	0.080	0.272
YOLO 11m	20.0	67.7	0.350	0.203	0.098	0.312
YOLO 12n[57]	2.6	6.3	0.259	0.142	0.057	0.224
YOLO 12s	9.2	21.2	0.312	0.176	0.081	0.274
YOLO 12m	20.1	67.2	0.336	0.192	0.094	0.298
YOLO 13n[58]	2.5	6.2	0.244	0.133	0.055	0.210
YOLO 13s	9.0	20.1	0.297	0.167	0.077	0.258
YOLOX-Tiny[59]	5.0	7.6	0.278	0.148	0.076	0.221
RT-DETR-R18	20.0	60.0	0.333	0.185	0.139	0.275
ATSS-R50[60]	38.9	110.0	0.338	0.204	0.100	0.317
Cascade-RCNN-R50[61]	69.3	236.0	0.326	0.197	0.099	0.309
D-Fine-N[62]	3.7	7.1	0.334	0.183	0.093	0.270
Faster-RCNN-R50[63]	41.4	208.0	0.329	0.194	0.095	0.309
FBRT-YOLO-M[64]	7.4	58.7	0.344	0.196	0.094	0.309
FBRT-YOLO-N	0.8	6.7	0.265	0.148	0.062	0.234
FBRT-YOLO-S	2.9	22.9	0.323	0.183	0.085	0.283
FFCA-YOLO[55]	7.1	51.4	0.267	0.122	0.091	0.295
RetinaNet-R50[54]	36.5	210.0	0.276	0.164	0.060	0.274
RTMDet-Tiny[65]	4.9	8.0	0.312	0.184	0.077	0.288
TOOD-R50[66]	32.0	199.0	0.339	0.204	0.102	0.317
TinyDef-DETR	20.5	65.0	0.372	0.217	0.148	0.348

5. Conclusions

In this paper, we proposed TinyDef-DETR, a DETR-based framework tailored for defect detection in UAV imagery of transmission lines. By integrating an Edge-Enhanced ResNet backbone, a stride-free space-to-depth module, a cross-stage dual-domain multi-scale attention mechanism, and a Focaler-Wise-SIoU regression loss, the model effectively addresses the challenges posed by small, ambiguous, and background-cluttered defects.

Extensive experiments on the CSG-ADCD dataset, as well as real-world UAV imagery, demonstrated that TinyDef-DETR consistently outperforms representative detectors in terms of detection accuracy, recall, and robustness, while maintaining computational efficiency. Ablation studies further verified the effectiveness of each proposed component, highlighting their complementary contributions to the overall performance.

The results confirm that TinyDef-DETR not only achieves strong detection capability for small and difficult objects but also provides a practical and efficient solution for real-world UAV-based inspection scenarios. Given its modular and lightweight design, the proposed framework holds promise for broader applications in power system inspection and can be extended to other small-object detection tasks in aerial remote sensing.

Author Contributions: Conceptualization, J.C. and S.Z.; methodology, J.C.; software, J.C.; validation, J.C. and F.S.; formal analysis, J.C.; investigation, J.C. and W.L.; resources, F.S. and S.Z.; data curation, J.C.; writing—original draft preparation, J.C.; writing—review and editing, S.Z. and F.S.; visualization, J.C.; supervision, S.Z.; project administration, S.Z.; funding acquisition, S.Z. All authors have read and agreed to the published version of the manuscript.

Funding: This work was supported by the National Natural Science Foundation of China under Grant 61673128, Grant 61573117, and Grant 41627801. (Corresponding author: Feng Shen.)

Institutional Review Board Statement: Not applicable.

Informed Consent Statement: Not applicable.

Data Availability Statement: Due to confidentiality agreements, part of the dataset used in this study cannot be shared publicly. However, the data presented in this study also include openly available resources from the VisDrone benchmark dataset, which can be accessed at <https://github.com/VisDrone/VisDrone-Dataset>, as described in [48].

Acknowledgments: The authors would like to thank the organizers of the VisDrone dataset for providing the publicly available data that supported this research. The authors also thank the developers of RT-DETR and MMDetection for their open-source contributions, which greatly facilitated the experiments in this work.

Conflicts of Interest: The authors declare no conflicts of interest.

References

1. Yang, L.; Fan, J.; Liu, Y.; Li, E.; Peng, J.; Liang, Z. A Review on State-of-the-Art Power Line Inspection Techniques. *IEEE Transactions on Instrumentation and Measurement* **2020**, *69*, 9350–9365.
2. Liu, X.; Miao, X.; Jiang, H.; Chen, J. Data Analysis in Visual Power Line Inspection: An in-Depth Review of Deep Learning for Component Detection and Fault Diagnosis. *Annual Reviews in Control* **2020**, *50*, 253–277.
3. Cheng, Y.; Liu, D. AdIn-DETR: Adapting Detection Transformer for End-to-End Real-Time Power Line Insulator Defect Detection. *IEEE Trans. Instrum. Meas.* **2024**, *73*, 1–11.
4. Yang, Y.; Wang, X. Recognition of Bird Nests on Transmission Lines Based on YOLOv5 and DETR Using Small Samples. *Energy Reports* **2023**, *9*, 6219–6226.
5. Mohsan, S.A.H.; Khan, M.A.; Noor, F.; Ullah, I.; Alsharif, M.H. Towards the Unmanned Aerial Vehicles (UAVs): A Comprehensive Review. *Drones* **2022**, *6*, 147.
6. Ahmed, F.; Mohanta, J.C.; Keshari, A. Power Transmission Line Inspections: Methods, Challenges, Current Status and Usage of Unmanned Aerial Systems. *J Intell Robot Syst* **2024**, *110*, 54.
7. Mirzaei, B.; Nezamabadi-pour, H.; Raouf, A.; Derakhshani, R. Small Object Detection and Tracking: A Comprehensive Review. *Sensors* **2023**, *23*, 6887.
8. Deng, X.; He, M.; Zheng, J.; Qin, L.; Liu, K. Research Progress on Power Visual Detection of Overhead Line Bolt Defects Based on UAV Images. *Drones* **2024**, *8*, 442.
9. Li, Y.; Liu, M.; Li, Z.; Jiang, X. CSSAdet: Real-Time End-to-End Small Object Detection for Power Transmission Line Inspection. *IEEE Trans. Power Delivery* **2023**, *38*, 4432–4442.
10. Redmon, J.; Divvala, S.; Girshick, R.; Farhadi, A. You Only Look Once: Unified, Real-Time Object Detection. In Proceedings of the 2016 IEEE Conference on Computer Vision and Pattern Recognition (CVPR), Las Vegas, NV, USA, 2016; pp. 779–788.
11. Zhang, H.; Li, F.; Liu, S.; Zhang, L.; Su, H.; Zhu, J.; Ni, L.; Shum, H.Y. DINO: DETR with Improved DeNoising Anchor Boxes for End-to-End Object Detection. In Proceedings of the The Eleventh International Conference on Learning Representations, 2022.
12. Zhao, Y.; Lv, W.; Xu, S.; Wei, J.; Wang, G.; Dang, Q.; Liu, Y.; Chen, J. DETRs Beat YOLOs on Real-time Object Detection. In Proceedings of the 2024 IEEE/CVF Conference on Computer Vision and Pattern Recognition (CVPR), Seattle, WA, USA, 2024; pp. 16965–16974.
13. Lin, T.Y.; Maire, M.; Belongie, S.; Hays, J.; Perona, P.; Ramanan, D.; Dollár, P.; Zitnick, C.L. Microsoft COCO: Common Objects in Context. In *Computer Vision – ECCV 2014*; Fleet, D.; Pajdla, T.; Schiele, B.; Tuytelaars, T., Eds.; Springer International Publishing: Cham, 2014; Vol. 8693, pp. 740–755.
14. Liu, Y.; Liu, D.; Huang, X.; Li, C. Insulator Defect Detection with Deep Learning: A Survey. *IET Generation Trans & Dist* **2023**, *17*, 3541–3558.
15. Deng, X.; He, M.; Zheng, J.; Qin, L.; Liu, K. Research Progress on Power Visual Detection of Overhead Line Bolt Defects Based on UAV Images. *Drones* **2024**, *8*, 442.
16. Vaswani, A.; Shazeer, N.; Parmar, N.; Uszkoreit, J.; Jones, L.; Gomez, A.N.; ukasz Kaiser, L.; Polosukhin, I. Attention Is All You Need. In Proceedings of the Advances in Neural Information Processing Systems. Curran Associates, Inc., 2017, Vol. 30.
17. Tian, Y.; Ahmad, R.B.; Abdullah, N.A.B. Accurate and Efficient Insulator Maintenance: A DETR Algorithm for Drone Imagery. *PLoS ONE* **2025**, *20*, e0318225.

18. Cheng, Y.; Liu, D. An Image-Based Deep Learning Approach with Improved DETR for Power Line Insulator Defect Detection. *Journal of Sensors* **2022**, *2022*, 1–22.
19. Wang, X.; Yang, T.; Zou, Y. Enhancing Grid Reliability through Advanced Insulator Defect Identification. *PLoS ONE* **2024**, *19*, e0307684.
20. Xie, Z.; Dong, C.; Zhang, K.; Wang, J.; Xiao, Y.; Guo, X.; Zhao, Z.; Shi, C.; Zhao, W. Power-DETR: End-to-end Power Line Defect Components Detection Based on Contrastive Denoising and Hybrid Label Assignment. *IET Generation Trans & Dist* **2024**, *18*, 3264–3277.
21. Shao, X.; Diao, S.; Li, L.; Zhao, X.; Mei, Y.; Zhu, Z. WT-DETR: Wavelet-enhanced DETR for Robust Tiny Object Detection via Multi-Scale Feature Optimization. *JOURNAL OF REAL-TIME IMAGE PROCESSING* **2025**, *22*.
22. Feng, D.; Xu, J.; Li, K.; Ma, Z.; Li, W.; Wang, D. FADet: A Frequency-Aware Detection Framework for Infrared Small Target Detection. *IEEE JOURNAL OF SELECTED TOPICS IN APPLIED EARTH OBSERVATIONS AND REMOTE SENSING* **2025**, *18*, 24963–24975.
23. Xu, W.; Ding, Z.; Wang, Z.; Cui, Z.; Hu, Y.; Jiang, F. Think Locally and Act Globally: A Frequency-Spatial Fusion Network for Infrared Small Target Detection. *IEEE TRANSACTIONS ON GEOSCIENCE AND REMOTE SENSING* **2025**, *63*.
24. Li, H.; Peng, X.; Zhang, J. FSCNet: Feature Synthesis with Wavelet Coefficients for Infrared Small Target Detection. *INFRARED PHYSICS & TECHNOLOGY* **2025**, *147*.
25. Wang, K.; Suo, B.; Zhang, G.; Yang, Y.; Qian, W. Small Object Detection Based on Spatial-Frequency Separated Cross-Attention Swin Transformer. *LASER & OPTOELECTRONICS PROGRESS* **2025**, *62*.
26. Chen, T.; Ye, Z. FreqODEs: Frequency Neural ODE Networks for Infrared Small Target Detection. *IEEE TRANSACTIONS ON GEOSCIENCE AND REMOTE SENSING* **2024**, *62*.
27. Luo, Z.; Wang, Y.; Chen, L.; Yang, W. Frequency Spectrum Features Modeling for Real-Time Tiny Object Detection in Remote Sensing Image. *IEEE GEOSCIENCE AND REMOTE SENSING LETTERS* **2024**, *21*.
28. Li, H.; Yang, J.; Xu, Y.; Wang, R. Mitigate Target-Level Insensitivity of Infrared Small Target Detection via Posterior Distribution Modeling. *IEEE JOURNAL OF SELECTED TOPICS IN APPLIED EARTH OBSERVATIONS AND REMOTE SENSING* **2024**, *17*, 13188–13201.
29. Liu, G.; Liu, S.; Wang, F.; Ma, J. Infrared Aerial Small Target Detection with NSCT and Two-Dimensional Property Histogram. *INTERNATIONAL JOURNAL OF PATTERN RECOGNITION AND ARTIFICIAL INTELLIGENCE* **2018**, *32*.
30. Guo, H.; Wu, Q.; Wang, Y. AUHF-DETR: A Lightweight Transformer with Spatial Attention and Wavelet Convolution for Embedded UAV Small Object Detection. *REMOTE SENSING* **2025**, *17*.
31. Suvittawat, N.; Kurniawan, C.; Datephanyawat, J.; Tay, J.; Liu, Z.; Soh, D.W.; Antunes Ribeiro, N. Advances in Aircraft Skin Defect Detection Using Computer Vision: A Survey and Comparison of YOLOv9 and RT-DETR Performance, 2025.
32. He, K.; Zhang, X.; Ren, S.; Sun, J. Deep Residual Learning for Image Recognition. In Proceedings of the 2016 IEEE Conference on Computer Vision and Pattern Recognition (CVPR), Las Vegas, NV, USA, 2016; pp. 770–778.
33. Vijayakumar, A.; Vairavasundaram, S. YOLO-based Object Detection Models: A Review and Its Applications. *Multimed Tools Appl* **2024**, *83*, 83535–83574.
34. Ismail, M.S.; Samad, R.; Pebrianti, D.; Mustafa, M.; Hasma Abdullah, N.R. Comparative Analysis of Deep Learning Models for Sheep Detection in Aerial Imagery. In Proceedings of the 2024 9th International Conference on Mechatronics Engineering (ICOM), Kuala Lumpur, Malaysia, 2024; pp. 234–239.
35. Redmon, J.; Farhadi, A. YOLOv3: An Incremental Improvement, 2018, [[arXiv:cs/1804.02767](https://arxiv.org/abs/1804.02767)].
36. Wang, C.Y.; Bochkovskiy, A.; Liao, H.Y.M. YOLOv7: Trainable Bag-of-Freebies Sets New State-of-the-Art for Real-Time Object Detectors. In Proceedings of the 2023 IEEE/CVF Conference on Computer Vision and Pattern Recognition (CVPR), Vancouver, BC, Canada, 2023; pp. 7464–7475.
37. Khanam, R.; Hussain, M. YOLOv11: An Overview of the Key Architectural Enhancements, 2024, [[arXiv:cs/2410.17725](https://arxiv.org/abs/2410.17725)].
38. Wang, Y.; Liu, J.; Zhao, J.; Li, Z.; Yan, Y.; Yan, X.; Xu, F.; Li, F. LCSC-UAVNet: A High-Precision and Lightweight Model for Small-Object Identification and Detection in Maritime UAV Perspective. *Drones* **2025**, *9*, 100.
39. Sunkara, R.; Luo, T. No More Strided Convolutions or Pooling: A New CNN Building Block for Low-Resolution Images and Small Objects. In Proceedings of the Machine Learning and Knowledge Discovery in Databases; Amini, M.R.; Canu, S.; Fischer, A.; Guns, T.; Kralj Novak, P.; Tsoumakas, G., Eds., Cham, 2023; pp. 443–459.
40. Finder, S.E.; Amoyal, R.; Treister, E.; Freifeld, O. Wavelet Convolutions for Large Receptive Fields. In *Computer Vision – ECCV 2024*; Leonardis, A.; Ricci, E.; Roth, S.; Russakovsky, O.; Sattler, T.; Varol, G., Eds.; Springer Nature Switzerland: Cham, 2025; Vol. 15112, pp. 363–380.
41. Zhou, H.; Sun, Z.; Sun, K. A UAV Image Small Object Detection Approach with Enhanced Feature Pyramid and Receptive Field. *Cluster Comput* **2025**, *28*, 714.

42. Rezatofighi, H.; Tsoi, N.; Gwak, J.; Sadeghian, A.; Reid, I.; Savarese, S. Generalized Intersection Over Union: A Metric and a Loss for Bounding Box Regression. In Proceedings of the 2019 IEEE/CVF Conference on Computer Vision and Pattern Recognition (CVPR), Long Beach, CA, USA, 2019; pp. 658–666.
43. Zheng, Z.; Wang, P.; Liu, W.; Li, J.; Ye, R.; Ren, D. Distance-IoU Loss: Faster and Better Learning for Bounding Box Regression. *Proceedings of the AAAI Conference on Artificial Intelligence* **2020**, *34*, 12993–13000.
44. Zheng, Z.; Wang, P.; Ren, D.; Liu, W.; Ye, R.; Hu, Q.; Zuo, W. Enhancing Geometric Factors in Model Learning and Inference for Object Detection and Instance Segmentation. *IEEE Transactions on Cybernetics* **2022**, *52*, 8574–8586.
45. Gevorgyan, Z. SloU Loss: More Powerful Learning for Bounding Box Regression, 2022, [[arXiv:cs/2205.12740](https://arxiv.org/abs/2205.12740)].
46. Zhang, H.; Zhang, S. Focaler-IoU: More Focused Intersection over Union Loss, 2024, [[arXiv:cs/2401.10525](https://arxiv.org/abs/2401.10525)].
47. Tong, Z.; Chen, Y.; Xu, Z.; Yu, R. Wise-IoU: Bounding Box Regression Loss with Dynamic Focusing Mechanism, 2023, [[arXiv:cs/2301.10051](https://arxiv.org/abs/2301.10051)].
48. Du, D.; Zhu, P.; Wen, L.; Bian, X.; Ling, H.; Hu, Q.; Peng, T.; Zheng, J.; Wang, X.; Zhang, Y.; et al. VisDrone-DET2019: The Vision Meets Drone Object Detection in Image Challenge Results. In Proceedings of the 2019 IEEE/CVF INTERNATIONAL CONFERENCE ON COMPUTER VISION WORKSHOPS (ICCVW), Seoul, SOUTH KOREA, 2019; IEEE International Conference on Computer Vision Workshops, pp. 213–226.
49. Chen, K.; Wang, J.; Pang, J.; Cao, Y.; Xiong, Y.; Li, X.; Sun, S.; Feng, W.; Liu, Z.; Xu, J.; et al. MMDetection: Open MMLab Detection Toolbox and Benchmark, 2019, [[arXiv:cs/1906.07155](https://arxiv.org/abs/1906.07155)].
50. Wang, A.; Chen, H.; Liu, L.; Chen, K.; Lin, Z.; Han, J.; Ding, G. YOLOv10: Real-Time End-to-End Object Detection. In Proceedings of the Proceedings of the 38th International Conference on Neural Information Processing Systems, Red Hook, NY, USA, 2025; Vol. 37, *NIPS '24*, pp. 107984–108011.
51. Khanam, R.; Hussain, M. YOLOv11: An Overview of the Key Architectural Enhancements, 2024, [[arXiv:cs/2410.17725](https://arxiv.org/abs/2410.17725)].
52. Meng, D.; Chen, X.; Fan, Z.; Zeng, G.; Li, H.; Yuan, Y.; Sun, L.; Wang, J. Conditional DETR for Fast Training Convergence, 2023, [[arXiv:cs/2108.06152](https://arxiv.org/abs/2108.06152)].
53. Carion, N.; Massa, F.; Synnaeve, G.; Usunier, N.; Kirillov, A.; Zagoruyko, S. End-to-End Object Detection with Transformers. In *Computer Vision – ECCV 2020*; Vedaldi, A.; Bischof, H.; Brox, T.; Frahm, J.M., Eds.; Springer International Publishing: Cham, 2020; Vol. 12346, pp. 213–229.
54. Lin, T.Y.; Goyal, P.; Girshick, R.; He, K.; Dollár, P. Focal Loss for Dense Object Detection, 2018, [[arXiv:cs/1708.02002](https://arxiv.org/abs/1708.02002)].
55. Zhang, Y.; Ye, M.; Zhu, G.; Liu, Y.; Guo, P.; Yan, J. FFCA-YOLO for Small Object Detection in Remote Sensing Images. *IEEE Trans. Geosci. Remote Sensing* **2024**, *62*, 1–15.
56. Meng, D.; Chen, X.; Fan, Z.; Zeng, G.; Li, H.; Yuan, Y.; Sun, L.; Wang, J. Conditional DETR for Fast Training Convergence. In Proceedings of the 2021 IEEE/CVF International Conference on Computer Vision (ICCV), Montreal, QC, Canada, 2021; pp. 3631–3640.
57. Tian, Y.; Ye, Q.; Doermann, D. YOLOv12: Attention-Centric Real-Time Object Detectors, 2025, [[arXiv:cs/2502.12524](https://arxiv.org/abs/2502.12524)].
58. Lei, M.; Li, S.; Wu, Y.; Hu, H.; Zhou, Y.; Zheng, X.; Ding, G.; Du, S.; Wu, Z.; Gao, Y. YOLOv13: Real-Time Object Detection with Hypergraph-Enhanced Adaptive Visual Perception, 2025, [[arXiv:cs/2506.17733](https://arxiv.org/abs/2506.17733)].
59. Ge, Z.; Liu, S.; Wang, F.; Li, Z.; Sun, J. YOLOX: Exceeding YOLO Series in 2021, 2021, [[arXiv:cs/2107.08430](https://arxiv.org/abs/2107.08430)].
60. Zhang, S.; Chi, C.; Yao, Y.; Lei, Z.; Li, S.Z. Bridging the Gap Between Anchor-based and Anchor-free Detection via Adaptive Training Sample Selection Between Anchor-Based and Anchor-Free Detection via Adaptive Training Sample Selection. In Proceedings of the Proceedings of the IEEE/CVF Conference on Computer Vision and Pattern Recognition, 2020, pp. 9759–9768.
61. Cai, Z.; Vasconcelos, N. Cascade R-CNN: High Quality Object Detection and Instance Segmentation. *IEEE Transactions on Pattern Analysis and Machine Intelligence* **2021**, *43*, 1483–1498.
62. Peng, Y.; Li, H.; Wu, P.; Zhang, Y.; Sun, X.; Wu, F. D-FINE: Redefine Regression Task in DETRs as Fine-grained Distribution Refinement, 2024, [[arXiv:cs/2410.13842](https://arxiv.org/abs/2410.13842)].
63. Ren, S.; He, K.; Girshick, R.; Sun, J. Faster R-CNN: Towards Real-Time Object Detection with Region Proposal Networks. In Proceedings of the Advances in Neural Information Processing Systems. Curran Associates, Inc., 2015, Vol. 28.
64. Xiao, Y.; Xu, T.; Xin, Y.; Li, J. FBRT-YOLO: Faster and Better for Real-Time Aerial Image Detection.
65. Lyu, C.; Zhang, W.; Huang, H.; Zhou, Y.; Wang, Y.; Liu, Y.; Zhang, S.; Chen, K. RTMDet: An Empirical Study of Designing Real-Time Object Detectors, 2022, [[arXiv:cs/2212.07784](https://arxiv.org/abs/2212.07784)].
66. Feng, C.; Zhong, Y.; Gao, Y.; Scott, M.R.; Huang, W. TOOD: Task-aligned One-stage Object Detection. In Proceedings of the 2021 IEEE/CVF International Conference on Computer Vision (ICCV), Montreal, QC, Canada, 2021; pp. 3490–3499.

Disclaimer/Publisher’s Note: The statements, opinions and data contained in all publications are solely those of the individual author(s) and contributor(s) and not of MDPI and/or the editor(s). MDPI and/or the editor(s) disclaim responsibility for any injury to people or property resulting from any ideas, methods, instructions or products referred to in the content.